Manuscript Details

Manuscript number	JNM_2018_388_R1
Title	Si-rich phases and their distributions in the oxide scale formed on 304 stainless steel at high temperatures
Article type	Full Length Article

Abstract

Si-rich phases and their distributions in the oxide scale formed on 304 stainless steel (304SS) kinetically affects SiO2 volatilization for the formation of silicate-based Cs-bearing microparticles released during the Fukushima Daiichi Nuclear Power Plant accident. Therefore, we investigated Si-rich phases and their distributions in the oxide scale on 304SS oxidized in H2O–H2 mixtures over the temperature range 1000–1300 ºC. SiO2 film stays at the base of the Cr2O3-type scale formed at low temperatures or high H2 contents in steam. Fe2SiO2 phase is non-uniformly distributed in the spinel-type scale formed under opposite conditions. Fe2SiO2 accumulation in the spinel-type scale is attributed to its thermodynamically metastable state in H2O–H2 mixtures. With increasing oxidation time, Fe2SiO2 phase was further oxidized into SiO2 phase.

Manuscript category	Nuclear materials, fuels and waste materials
Corresponding Author	Lichun Zheng
Corresponding Author's Institution	Tohoku University
Order of Authors	Lichun Zheng, Kazuya Hosoi, Shigeru Ueda, Xu Gao, Shin-ya Kitamura, Yoshinao Kobayashi
Suggested reviewers	Yukihiko Satou, Xiangyu Zhong, Bronislava Gorr

Submission Files Included in this PDF

File Name [File Type]

Cover letter.docx [Cover Letter]

Reply to the editors and reviewers.docx [Response to Reviewers]

Manuscript with changes marked.doc [Revised Manuscript with Changes Marked]

Highlights.docx [Highlights]

Clean manuscript.doc [Manuscript File]

Figure 1.tif [Figure]

Figure 2.tif [Figure]

Figure 3.tif [Figure]

Figure 4.tif [Figure]

Figure 5.tif [Figure]

Figure 6.tif [Figure]

Figure 7.tif [Figure]

Figure 8.tif [Figure]

Figure 9.tif [Figure]

Figure 10.tif [Figure]

Figure 11.tif [Figure]

Figure 12.tif [Figure]

Figure 13.tif [Figure]

Figure 14.tif [Figure]

Figure 15.tif [Figure]

Figure 16.tif [Figure]

Figure 17.tif [Figure]

Figure 18.tif [Figure]

Figure 19.tif [Figure]

Figure 20.tif [Figure]

To view all the submission files, including those not included in the PDF, click on the manuscript title on your EVISE Homepage, then click 'Download zip file'.

Research Data Related to this Submission

There are no linked research data sets for this submission. The following reason is given:
Data will be made available on request

Si-rich phases and their distributions in the oxide scale formed on 304 stainless steel at high temperatures

Lichun Zheng[a,□], Kazuya Hosoi[a], Shigeru Ueda[a], Xu Gao[a], Shin-ya Kitamura[a], Yoshinao Kobayashi[b]

[a] Institute of Multidisciplinary Research for Advanced Materials, Tohoku University, Katahira 2-1-1, Aoba-ku, Sendai 980-8577, Japan

[b] Laboratory for Advanced Nuclear Energy, Institute of Innovative Research, Tokyo Institute of Technology, Ookayama 2-12-1, Meguro-ku, Tokyo 152-8550, Japan

Abstract−Si-rich phases and their distributions in the oxide scale formed on 304 stainless steel (304SS) kinetically affects SiO_2 volatilization for the formation of silicate-based Cs-bearing microparticles released during the Fukushima Daiichi Nuclear Power Plant accident. Therefore, we investigated Si-rich phases and their distributions in the oxide scale on 304SS oxidized in H_2O–H_2 mixtures over the temperature range 1000–1300 ºC. SiO_2 film stays at the base of the Cr_2O_3-type scale formed at low temperatures or high H_2 contents in steam. Fe_2SiO_2 phase is non-uniformly distributed in the spinel-type scale formed under opposite conditions. Fe_2SiO_2 accumulation in the spinel-type scale is attributed to its thermodynamically metastable state in H_2O–H_2 mixtures. With increasing oxidation time, Fe_2SiO_2 phase was further oxidized into SiO_2 phase.

Keywords: 304 stainless steel; Oxidation; High temperatures; Si distribution; SiO_2; Fe_2SiO_4

1. Introduction

A huge amount of radioactive materials were released into the environment during the Fukushima Daiichi Nuclear Power Plant (FDNPP) accident initiated by the tsunami following the Great East Japan Earthquake on 11 March 2011, causing severe radioactive contamination in Northeast Japan. Radioactive Cs including ^{134}Cs and ^{137}Cs is one of the most abundant and active radionuclides generated in nuclear reactors through fission reactions [1]. Except water-soluble Cs-bearing microparticles [2], two types of water-insoluble Cs-bearing microparticles, i.e., spherical and non-spherical, have been reported [3–9]. Adachi *et al.* [3] first analyzed the spherical Cs-bearing microparticles collected in Tsukuba located 170 km southwest of FDNPP using scanning electron microscope (SEM), revealing Cs, Fe, Zn, Mn, Cl and O elements in the microparticles. Abe *et al.*

[4], using synchrotron radiation X-ray analyses, found that the spherical Cs-bearing microparticles contain radioactive U along with Cs, and that the microparticles have a glass-like structure. Presence of Si in the microparticles was not confirmed in the studies by Adachi *et al.* [3] and Abe *et al*. [4] due to the use of Si-containing sample substrates. Kogure *et al.* [5] and Yamaguchi *et al.* [6] performed further characterization on the spherical microparticles collected in Fukushima using scanning transmission electron microscope (STEM) and revealed their silicate matrix containing substantial elements of Cs, Fe, Zn, Sn, K, Rb, Cu, Mo, Cl, S, and Te. Fe and Zn are homogeneously distributed in the microparticles while most other elements vary radially especially for large microparticles [5,6]. The non-spherical Cs-bearing microparticles, both single particles and aggregates, were collected in Fukushima and analyzed by Satou *et al.* [7], Yamaguchi *et al.* [8] and Higaki *et al.* [9]. The non-spherical microparticles have similar main components as the spherical microparticles but contain more minor elements, such as Cr, Ni, Al, Ti and Ca.

Since SiO_2 forms the matrix of the Cs-bearing microparticles [5,6], one of the most concerning issues is SiO_2 origin. Kogure *et al.* [5] suggested that SiO_2 may come from glass fibers used in heat insulators covering the pipes for water coming in and out of reactor pressure vessel (RPV) or from concrete structures located at the bottom of the containment vessel. However, both glass fibers and concrete structures contain substantial amounts of Ca and Al, which are absent in most observed Cs-bearing microparticles. Ogawa *et al.* [10] proposed the possibility of SiO_2 volatilization from Si-containing steels used in nuclear reactors as control rod claddings and tie plates supporting fuel rods, and subsequent deposition during which Cs and other elements are incorporated into SiO_2 by diffusion. The proposal by Ogawa *et al.* [10] seems more reasonable as SiO_2 volatilization in steam and hydrogen atmospheres has been widely reported in many research fields [11–13]. Currently, this proposal is under further study by other investigators [14,15]. A. Suzuki [15] simulated Cs-bearing microparticle formation via SiO_2 volatilization and deposition using SiO_2 + Cs_2CO_3 powders and soda-lime glass + Cs_2CO_3 powder heated in H_2O–Ar and H_2O–H_2 atmospheres in the temperature range 1200-1600 ºC and observed that the size and morphology of deposited SiO_2 microparticles strongly depend on atmosphere and temperature.

Small additions of Si have long been known to improve oxidation resistance of stainless steels. Upon oxidation, SiO_2 or Fe_2SiO_4 phase is formed in the oxide scale with different distributions, depending on Si content, steel composition, atmosphere, temperature and other factors [16–26]. Apparently, Si-rich phases and their distributions in the oxide scale kinetically affect SiO_2 volatilization and thus Cs-bearing microparticle formation. Therefore, for better understanding SiO_2

volatilization from Si-containing steels, sufficient knowledge on Si-rich phases and their distributions in the oxide scale formed on the steels is required. 304 stainless steel (304SS) containing around 1 wt.% Si is used in nuclear reactors as control rod claddings containing B_4C powder or pellets. At temperatures below 1000 ºC, Cr_2O_3-type scale is formed upon oxidation and SiO_2 phase as a thin film stays at the base of the scale, when Si content is high enough [18,19,24,27–29]. At higher temperatures, $(Fe,Cr,Ni)_3O_4$ spinel-type scale is formed [30–32]. However, Si-rich phases and their distributions in the spinel-type scale are unclear. Therefore, in this article, we studied Si-rich phases and their distributions in the oxide scale on 304SS oxidized in H_2O–H_2 mixtures in the temperature range 1000–1300 ºC. The temperature is limited to 1300 ºC because rapid liquefaction of 304SS with B_4C due to eutectic reaction occurs at temperatures above 1250 ºC [33].

2. Experimental

2.1. Materials

To prepare 304SS specimens, 304SS ingot was first produced by melting high purity Fe, Ni, Cr, Mn, Si, FeP and Fe–1.24%Mn–0.19%Si–0.22%C alloy three times in argon atmosphere using arc furnace. Then the ingot was forged at 1200 ºC, cold-rolled, and heat treated at 1050 ºC for 30 min, followed by rapid quenching. The chemical composition of obtained steel sheet was analysed and listed in **Table 1**. Plate-like specimens (2×10×10 mm) cut from the steel sheet were ground with 1200 grit SiC paper, rinsed with deionized water, cleaned ultrasonically in acetone, and dried before experiments.

Table 1 Chemical composition of 304SS investigated, wt.%.

Cr	Ni	Mn	Si	P	S	C	Fe
19.02	9.49	1.14	0.96	0.028	0.002	0.042	Bal.

2.2. Non-isothermal oxidation

To determine characteristic temperatures for later isothermal oxidation, non-isothermal oxidation of 304SS in the temperature range 750–1250 ºC was performed using a thermobalance (SII TG/DTA6300N). Since the thermobalance is not designed to work in steam atmosphere, pure CO_2 was used instead of steam. Oxygen potential in CO_2 atmosphere is almost the same as that in steam atmosphere over the investigated temperature range [34]. Before 750 ºC, the specimen (1.5×2.0×4.2

mm^3) was heated at 20 ºC□min^{-1} in argon atmosphere (100 ml□min^{-1}). After 750 ºC, the heating rate was decreased to 2 ºC□min^{-1} and the atmosphere was switched to CO_2 (100 ml□min^{-1}).

2.3. Isothermal oxidation

Isothermal oxidation of 304SS in H_2O–H_2 mixtures was performed in a SiC resistance-heated vertical tube furnace with an alumina reaction tube (diameter: 4.2 cm; length: 100 cm). The furnace was first heated to prescribed temperature under air and held there for 30 min. Then, a 304SS specimen hanged by a Pt wire was put into the furnace at a position of 10 cm away from the top of the furnace, where the temperature was measured around 60 ºC. To remove impurities, the reaction tube was purged with high purity argon gas at a flow rate of 2.8 L·min^{-1} for 10 min. Thereafter, the gas was switched to H_2O–H_2–Ar mixtures. 30 minutes later, the specimen was rapidly lowered to the hot zone of the furnace for isothermal oxidation. After a pre-set time, the specimen was rapidly taken out of the furnace and cooled in air. All gases used in this work are highly pure with impurities less than 0.3 ppm. The steam was generated by bubbling argon (300 ml·min^{-1}) through a boiler heated by a water bath at 70 ºC. The steam flow rate was measured off-line at 82 ml·min^{-1} at standard temperature and pressure for gas. The experimental conditions are listed in **Table 2**.

Table 2 Details of the experimental conditions.

Specimen No.	Temp. (ºC)	Time (min)	Q_{H_2O} (ml□min^{-1})	Q_{H_2} (ml□min^{-1})	f_{H_2} (vol.%)
T1-1	1000	120	82	0	0
T2-1	1150	60	82	0	0
T3-1	1200	60	82	0	0
T3-2	1200	90	82	0	0
T3-3	1200	120	82	0	0
T3-4	1200	180	82	0	0
T3-5	1200	60	82	10	11
T3-6	1200	60	82	80	49
T4-1	1300	60	82	0	0

2.4. Post-test examination

Before and after oxidation, the specimens were carefully weighted using a weighing scale accurate to 0.0001 g for obtaining their weight changes. Thereafter, oxidized specimens were mounted in epoxy resin to protect the oxide scales, cut vertically through the centre of the specimens,

mechanically ground and polished, and finally coated with carbon. Post-test examination of the oxide scales was performed with an electron probe micro-analyzer (FEG-EPMA JXA-8530F), equipped with wavelength dispersive spectrometers (WDS). The EPMA was operated at 15 kV voltage and 30 nA current. Fe and O elements were calibrated by standards of pure Fe_2O_3. Cr, Ni and Si elements were calibrated by standards of pure Cr, Ni and SiO_2. To measure oxide scale thickness, three micrographs for each specimen were taken using the EPMA in backscattered electrons (BSE) mode. Then, the micrographs were processed with an image analyser (Image-Pro Plus 7.0) to obtain oxide scale thickness.

3. Experimental results

3.1. Oxidation kinetics

Fig. 1 shows relative weight change of 304SS non-isothermally oxidized in CO_2 atmosphere over the temperature range of 750–1250 ºC. The relative weight change increases slowly and linearly with temperature up to around 1200 ºC. Thereafter, it increases sharply. This suggests that oxide scale quality deteriorates dramatically at temperatures ≥ 1200 ºC. This will be revealed in section 3.2.1. Based on the non-isothermal oxidation results, characteristic temperatures of 1000 ºC, 1150 ºC, 1200 ºC and 1300 ºC were chosen for further investigations.

Fig. 2 shows weight changes of 304SS isothermally oxidized at 1000 ºC, 1150 ºC, 1200 ºC and 1300 ºC in steam. As seen, weight changes are quite small at 1000 ºC and 1150 ºC but large at 1200 ºC and 1300 ºC. This is consistent with the non-isothermal oxidation results (Fig. 1). Fig. 3 shows weight change of 304SS as a function of time during isothermal oxidation at 1200 ºC in steam. Weight change first increases and then decreases with increasing time. Especially, weight change becomes negative at 180 min, clearly indicating that oxide scale spalled during oxidation. Severe oxide scale spallation was directly observed during cooling especially for the specimens oxidized in steam. Presence of residual stresses in the oxide scale and alloy may be responsible for oxide scale spallation during cooling [18]. Moreover, weight change decreases substantially with increasing H_2 content in steam at 1200 ºC. Additions of 11 vol.% and 49 vol.% H_2 in steam decrease weight change of 304SS to 1/3 and 1/9 of that in steam, respectively. This clearly indicates that H_2 favours the formation of protective oxide scale.

3.2. Microstructural analysis

3.2.1. Effect of temperature

To figure out temperature effect on oxide scale microstructure, 304SS was oxidized in steam at 1000 ºC, 1150 ºC, 1200 ºC and 1300 ºC. Fig. 4 shows oxide scale microstructure on 304SS oxidized in steam at 1000 ºC for 120 min. Two types of oxide scales were observed on the plate-like specimen. On one surface, most part of the oxide scale is dense and quite uniform in thickness (Fig. 4a). The oxide scale (spot 1) was identified as Cr_2O_3 by composition analysis (Table 3). The internal precipitates (spot 2) forming a non-continuous film at the metal-oxide interface were identified as SiO_2. As previously reported [16,18,20,29], SiO_2 intrusions were found to grow along the grain boundaries of metal matrix. On another surface, the oxide scale is mostly porous and non-uniform in thickness (Fig. 4b). The porous oxide scale (12.7 μm) is much thicker than the dense oxide scale (1.1 μm). The porous oxide scale exhibits a multilayer morphology. This is more clearly seen from elemental mappings given in Fig. 4c. The matrix of the porous oxide scale (spot 3) was identified as $(Fe,Cr)_3O_4$ spinel containing a trace amount of Ni. Si content in the spinel phase is around 0.7%, which is 0.3% lower than that in the metal matrix. The porous oxide scale contains many bright and dark particles. The bright particles (spot 4) were identified as Fe–Cr–Ni metallic phase containing less than 0.1% Si. The dark particles are rich in Si, as indicated by Si mapping (Fig. 4c). Their compositions, however, were not obtained as their sizes are smaller than the electron-beam interaction volume [39]. Possibly, the Si-rich phase is Fe_2SiO_4 based on Si-rich phase identification results in other specimens.

Table 3 Chemical compositions of the spots indicated by plus sign, at.%.

Spots	Fe	Cr	Ni	Si	O	Mn, Al, Ti	Comment
1	1.10	39.38	0.11	1.50	57.90	-	Cr_2O_3
2	20.25	4.27	1.51	23.93	50.05	-	SiO_2
3	23.76	2.68	71.16	0.09	2.31	-	$FeCr_{0.11}Ni_{2.99}$
4	16.73	24.40	0.21	0.92	57.74	-	$Fe_{1.22}Cr_{1.78}O_4$
5	28.36	2.38	0.24	13.17	55.85	-	Fe_2SiO_4
6	46.37	1.13	0.32	0.10	52.08	-	Fe_3O_4
7	44.28	0.59	0.31	0.03	54.79	-	Fe_2O_3
8	34.60	2.19	0.10	0.06	63.05	-	Fe_2O_3
9	21.26	21.36	0.11	0.02	57.26	-	$Fe_{1.50}Cr_{1.50}O_4$
10	1.59	37.50	0.12	0.10	60.69	-	Cr_2O_3
11	19.16	20.57	0.90	14.46	35.99	7.59, 0.91, 0.43	$MnSiO_3$+SiO_2
12	19.91	15.54	0.76	15.85	38.61	9.32, 0.01, 0	$MnSiO_3$+SiO_2
13	10.52	18.66	0.25	15.43	46.60	8.53, 0.01, 0	$MnSiO_3$+SiO_2+Cr_2O_3

14	31.09	7.25	3.86	19.56	38.10	0.09, 0.05, 0	SiO_2
15	0.99	37.63	0.19	0.36	60.82	-	Cr_2O_3
16	17.05	15.14	6.49	0.24	61.08	-	$Fe_{1.32}Cr_{1.18}Ni_{0.50}O_4$

Note: "-" indicates that Mn, Al, Ti elements were not measured due to their low contents.

Dense and porous oxide scales were observed on each surface of 304SS oxidized in steam at 1150 ºC for 60 min. The dense oxide scale is very similar to that in the specimen heated at 1000 ºC (Fig. 4a) and is therefore not shown here. The porous oxide scale shown in Fig. 5 has a double-layered structure. Again, the inner oxide scale was identified as $(Fe,Cr)_3O_4$ spinel, containing Si-rich phase and Fe–Cr–Ni metallic phase. Fe/Si ratio in the Si-rich phase (spot 5) was measured at 2.15. Considering the small size of the Si-rich phase, some collected Fe signal may come from surrounding spinel phase. Therefore, it is likely that the Si-rich phase is pure Fe_2SiO_4. The outer oxide scale mainly contains Fe and O, with trace amounts of Cr, Ni and Si. The inner region (spot 6) is close to Fe_3O_4 and outer region (spot 7) is close to Fe_2O_3. The outer Fe_2O_3 phase was likely transformed from Fe_3O_4 phase during cooling in air [32].

Dense and porous oxide scales were also formed on 304SS oxidized in steam at 1200 ºC for 60 min. The dense oxide scale was only observed on one surface of 304SS and occupied around 50% of the surface (Fig. 6). Different from the dense oxide scale observed at 1000 ºC and 1150 ºC (Fig. 4a), the dense oxide scale formed at 1200 ºC has three layers identified as Fe_2O_3 (spot 8), $(Fe,Cr)_3O_4$ spinel (spot 9) and Cr_2O_3 (spot 10), respectively. The outer two layers spalled severely, which possibly occurred during cooling. Fig. 7 shows the microstructure of the porous oxide scale. The double-layered oxide scale is similar to that in the specimen heated at 1150 ºC (Fig. 5). Again, partial oxidation of the outer oxide scale during cooling was inferred (Fig. 7a). The inner oxide scale, identified as $(Fe,Cr)_3O_4$ spinel, is full of lateral cracks. Chemical composition of the spinel phase varies with distance from the metal-oxide interface (Fig. 8). From the metal-oxide interface outward, Fe content in the spinel phase increases while Cr content decreases. This is consistent with the report by Bittel *et al.* [40]. Ni and especially of Si contents in the spinel phase are extremely low.

As in the specimen heated at 1150 ºC (Fig. 5), Fe–Ni–Cr metallic phase and Si-rich phase are distributed in the inner oxide scale. Chemical composition of the Fe–Cr–Ni metallic phase also varies with distance from the metal-oxide interface (Fig. 9). From the metal-oxide interface outward, Fe content in the metallic phase decreases from 72 wt.% to 37 wt.% while Ni content increases

from 9 wt.% to 62 wt.%. Cr content in the metallic phase keeps constant around 2 wt.%. Si content in the metallic phase is negligible. Variations of Fe, Cr and Ni contents in the metallic phase clearly show that selective oxidation occurred during oxidation of 304SS. Fe and Cr in 304SS were first oxidized at the metal-oxide interface, generating Fe- and Ni-rich Fe–Cr–Ni metallic phase there. As the oxidation proceeds, Fe in the metallic phase was further selectively oxidized, leading to lower Fe content and higher Ni content in the metallic phase. Note that oxidation of Ni in the metallic phase was insignificant as Ni content in inner oxide scale was insignificantly changed across the oxide scale (Fig. 8). Figs. 7b and 7c show enlarged views of Si-rich phase near the metal-oxide interface and near the spinel-spinel interface, respectively. In both regions, Si-rich phases were identified as Fe_2SiO_4. Fe_2SiO_4 phase significantly accumulates in the inner oxide scale (Fig. 7d). This phenomenon is insignificant at 1000 ºC (Fig. 4) and 1150 ºC (Fig. 5). Si is also enriched in the precipitates (dark colour) in the metal matrix (Fig. 7b). The Si-rich precipitates contain substantial amounts of Mn, Al and Ti. Mn, Al and Ti contents were found to vary significantly among the precipitates. Mostly, Mn content is the highest and Ti content is the lowest. The total amount of Mn, Al and Ti in the precipitates is around 6–9 at.% according to five measurements. The atomic ratio of O/(2Si+Mn) is very close to 1 (spot 11). Therefore, the Si-rich precipitates may be a mixture of $MnSiO_3$ and SiO_2 according to SiO_2–MnO phase diagram [41]. Al and Ti contents were not measured in the present 304SS due to their very low contents. Al and Ti contents in steel are usually in the range of hundreds of ppm.

Fig. 10 shows the microstructure of the oxide scale on 304SS oxidized in steam at 1300 ºC for 60 min. The inner oxide scale is quite compact. This is different from the cases at lower temperatures. Near the spinel-spinel interface, Fe_2SiO_4 phase was scarcely observed (Fig. 10c). Instead, the region is full of large pores. From spinel-spinel interface inward, Si content in the inner oxide scale gradually increases (Fig. 10d). The region near the metal-oxide interface has the highest Si content. Roughly, Si-poor region overlaps with Ni-rich region (Fig. 10e). Si-rich precipitates far away from the metal-oxide interface consist of $MnSiO_3$ and SiO_2 (spot 12). Some percentages of Cr_2O_3 may be incorporated in the precipitates closer to the metal-oxide interface (spot 13). This is a little bit different from the case at 1200 ºC, where presence of Cr_2O_3 in the Si-rich precipitates was not observed.

3.2.2. Effect of oxidation time

To investigate the effect of oxidation time on oxide scale microstructure, 304SS was oxidized at 1200 ºC for longer times, i.e., 90 min, 120 min and 180 min. Fig. 11 shows the microstructure of the

oxide scale on 304SS oxidized in steam at 1200 ºC for 90 min. The inner oxide scale becomes less porous, as compared with the case at 60 min (Fig. 7). This indicates that long oxidation time favours the formation of compact oxide scale. This occurred possibly due to that Fe and Cr diffused outward from the metal matrix and reacted with oxygen at the pores and cracks. Consequently, the pores and cracks observed at 60 min were closed. The inner oxide scale can be divided into three regions based on the distribution of Si-rich phase identified as Fe_2SiO_4. In region Ⅰ, Fe_2SiO_4 phase was scarcely observed (Fig. 11c). This region, however, contains lots of large pores. This phenomenon was similar to that observed at 1300 ºC (Fig. 10). Fe_2SiO_4 phase was concentrated into regions Ⅱ and Ⅲ. Region Ⅲ contains much more Fe_2SiO_4 phase than region Ⅱ. The interface between region Ⅱ and region Ⅲ was clearly seen (Fig. 11b). Large pores were occasionally observed in the two regions. The region near the metal-oxide interface has less Fe_2SiO_4 phase as compared with the central region (Fig. 11d). Si distribution in the inner oxide scale can also be seen from Si mapping (Fig. 11e). Si-rich precipitates in the metal matrix were identified as pure SiO_2 (spot 14). This is different from the case at 60 min.

Fig. 12 shows the microstructure of the oxide scale on 304SS oxidized in steam at 1200 ºC for 120 min. Due to severe spallation during oxidation, only part of the oxide scale detached from the metal matrix was collected (Fig. 12a). The inner oxide scale becomes more compact, as compared with the case at 90 min (Fig. 11). The Fe–Cr–Ni metallic phase observed in the previous specimens disappeared due to oxidation. Ni was incorporated into the inner oxide scale, forming $(Fe,Cr,Ni)_3O_4$ spinel phase. Si-rich phase identified as SiO_2 (Table 4) was only observed at the edge of the oxide segment, starting from where the oxide scale broke (Fig. 12c). Obviously, SiO_2 phase was transformed from Fe_2SiO_4 phase somewhere between 90 min and 120 min. SiO_2 particles in the oxide scale exist as aggregates (Fig. 12b). The morphology of single SiO_2 particles is irregular. The size of single SiO_2 particles is around 2 μm in diameter.

Table 4 Chemical composition of Si-rich phase averaged from 4 randomly selected spots in the inner oxide scale shown in Fig. 12, at.%.

	Fe	Cr	Si	O	Comment
Average	1.12	0.76	30.26	67.85	O/Si=2.24
S.D.	0.72	0.39	2.06	1.55	SiO_2

Except the oxide scale shown in Fig. 12, a thin and dense oxide scale completely covering the metal matrix was observed (Fig. 13). The oxide scale is non-uniform in thickness and composition. The inner subscale is Cr_2O_3 (spot 15) and the outer subscale is $(Fe,Cr,Ni)_3O_4$ spinel (spot 16). SiO_2 precipitates in the metal matrix are distributed in a wide region. This is distinct from that in the specimens heated at lower temperatures, where SiO_2 precipitates closely stay at the base of the dense oxide scale (Fig. 4a).

Fig. 14 shows the microstructure of the oxide scale on 304SS oxidized in steam at 1200 ºC for 180 min. Again, due to severe spallation, only part of the oxide scale covering the metal matrix was collected (Fig. 14a). In the inner region, the oxide scale looks quite dense. The outer region, however, is full of large cracks. Cr mapping suggests the presence of a Cr_2O_3 subscale near the metal-oxide interface (Fig. 14c). Si-rich phases in the oxide scale and in the metal matrix were both identified as SiO_2 (Fig. 14b). SiO_2 phase in the oxide scale was only occasionally observed (Figs. 14b and 14d). Distribution of SiO_2 precipitates in the metal matrix is in a similar manner as in the specimen heated for 120 min (Fig. 13).

3.2.3. Effect of H_2 content in steam

To investigate H_2 effect on oxide scale microstructure, 304SS was oxidized at 1200 ºC in H_2O–H_2 mixtures. Fig. 15 shows the microstructure of the oxide scale on 304SS oxidized in 89% H_2O–11% H_2 at 1200 ºC for 60 min. Due to severe spallation, only part of the oxide scale detached from the metal matrix was collected. Presence of H_2 in steam makes the oxide scale less porous, as compared with the oxide scale formed in steam (Fig. 7). Si-rich phase identified as Fe_2SiO_4 significantly accumulates in the oxide scale. A large region near the spinel-spinel interface contains almost no Fe_2SiO_4 phase but lots of pores. Similar phenomena were observed in the specimens heated in steam atmosphere (Figs. 10 and 11). The oxide scale on 304SS oxidized in 51% H_2O–49% H_2 at 1200 ºC for 60 min is mostly thin and dense. Porous oxide scale was occasionally observed. The dense oxide scale resembles that in the specimen heated in steam at 1000 ºC (Fig. 4a).

4. Discussion

4.1. Oxide scale types

Both spinel-type and Cr_2O_3-type scales were observed on 304SS, depending on temperature, H_2 content in steam and oxidation time (Table 5). Porous spinel-type scale was formed at high temperatures or low H_2 contents (Figs. 7, 10 and 15). Long oxidation times caused the formation of a dense Cr_2O_3-type subscale at the base of spinel-type scale (Figs. 13 and 14). On the contrary,

dense or partly dense Cr_2O_3-type scale was formed at low temperatures or high H_2 contents (Figs. 4 and 6), which is inconsistent with thermodynamic calculations that spinel-type rather than Cr_2O_3-type scale is formed on 304SS under all conditions investigated (Fig. 16). Note that equilibrium oxygen potentials for each reaction in Fig. 16 were calculated according to the below relationship:

$$\log\left(P_{O_2}\right) = \frac{\Delta G^{o}}{2.303RT} \tag{1}$$

where P_{O_2} is the equilibrium oxygen potential, ΔG^{o} is the standard Gibbs free energy, R is the universal gas constant and T is the absolute temperature.

When an alloy is exposed to an oxidizing atmosphere, oxide precipitates of all the alloy constitutes are formed at the bare surface of the alloy, roughly in proportion to their compositions [18]. For Cr-containing alloys, Cr_2O_3 precipitates are thermodynamically the most stable but Fe-rich precipitates are the fastest growing. To form a protective oxide scale, i.e., Cr_2O_3 oxide scale, a critical volume fraction of Cr_2O_3 precipitates is required to undercut the growth of Fe-rich precipitates. To form such a critical volume fraction of Cr_2O_3 precipitates, Cr content in Cr-containing alloys must exceed a critical value. The critical molar fraction of Cr (N_{Cr}) is expressed as: [42]

$$N_{Cr} = \left(\frac{2\pi g \;\; V_m \;\; N_O^S D_O}{3 \;\; V_{Cr_2O_3} \;\; D_{Cr}}\right)^{0.5} \tag{2}$$

where g is the critical volume fraction of Cr_2O_3 precipitates for transition from internal to external oxidation; V_m and $V_{Cr_2O_3}$ are the molar volumes of alloy and Cr_2O_3, respectively; N_O^S is the oxygen solubility in the alloy in equilibrium with oxygen potential at the metal-oxide interface; D_O and D_{Cr} are the diffusion coefficients of O and Cr in the alloy, respectively. Apparently, those conditions that decrease oxygen inward flux, e.g., lower N_O^S and D_O, and that increase Cr outward flux, e.g., higher D_{Cr}, favour the formation of external Cr_2O_3 scale instead of internal Cr_2O_3 precipitates. Both low temperatures and high H_2 contents generate low oxygen potentials in steam (Fig. 16) and thus low N_O^S values. This explains the formation of Cr_2O_3-type scale on 304SS oxidized at low temperatures or high H_2 contents. With the thickening of spinel-type scale, oxygen inward flux decreases, lowering the critical Cr content for Cr_2O_3-type scale formation. Therefore, a Cr_2O_3-type subscale may be formed at the base of spinel-type scale after long oxidation times, as observed in this work (Figs. 13 and 14) and in other studies [18,29,36,43]. By introducing in the alloy more grain boundaries acting as short-circuit diffusion paths, D_{Cr} can be significantly increased, favouring the formation of external Cr_2O_3 scale. Therefore, fine-grained alloys were reported to have better oxidation resistance [18,29,44,45]. For this reason, the mixture of dense and porous

oxide scales observed at 1000 ºC and 1150 ºC implies the non-uniform grain size at the surfaces of 304SS.

Table 5 Summary of oxide scales and Si-rich phases in the oxide scale.

Specimen No.	Temp. (ºC)	Time (min)	f_{H_2} (%)	Scale thickness (μm)	Scale types	Si-rich phases Observed	Si-rich phases Calculated
T1-1	1000	120	0	D=1.1, P=12.7	Cr_2O_3+Spinel	SiO_2+Fe_2SiO_4	SiO_2
T2-1	1150	60	0	D=6.8, P=38.5	Cr_2O_3+Spinel	SiO_2+Fe_2SiO_4	SiO_2
T3-1	1200	60	0	O=30.3, I=68.6	Spinel	SiO_2+Fe_2SiO_4	SiO_2
T3-2	1200	90	0	O=59.5, I=231.5	Spinel	Fe_2SiO_4	SiO_2
T3-3	1200	120	0	O=54.8, I=(52.3)	Cr_2O_3-Spinel	SiO_2	SiO_2
T3-4	1200	180	0	O=59.0, I=25.5	Cr_2O_3-Spinel	SiO_2	SiO_2
T3-5	1200	60	11	O=27.4, I=(52.7)	Spinel	Fe_2SiO_4	Fe_2SiO_4
T3-6	1200	60	49	D=2.4	Cr_2O_3	SiO_2	Fe_2SiO_4
T4-1	1300	60	0	O=(241.0), I=402.0	Spinel	Fe_2SiO_4	SiO_2

Note: I=Inner oxide scale, O=Outer oxide scale, D=Dense oxide scale, P=Porous oxide scale. Thicknesses of incomplete oxide scales are marked with parentheses.

4.2. Si-rich phase types

We observed different Si-rich phases, i.e., SiO_2 and Fe_2SiO_4, depending on the type of oxide scales formed on 304SS (Table 5). When Cr_2O_3-type scale is formed, a thin SiO_2 film with intrusions stays at the base of Cr_2O_3-type scale (Figs. 4a, 6, 13 and 14). No Si-rich phases were observed in the matrix of Cr_2O_3-type scale. On the contrary, when spinel-type scale is formed, Si-rich phases are distributed in the spinel-type scale as Fe_2SiO_4 (Figs. 4b, 5, 7, 10, 11 and 15) and in the metal matrix near the metal-oxide interface as pure SiO_2 (Fig. 11) or $MnSiO_3$-SiO_2 mixture (Figs. 7 and 10). Oxidation conditions determine oxide scale types. Therefore, which Si-rich phase is formed intrinsically depends on oxidation conditions. According to thermodynamic calculations, SiO_2 phase is stable in steam and Fe_2SiO_4 phase in H_2O–H_2 mixtures (Fig. 17). Obviously, experimental observations in most specimens are not in agreement with thermodynamic calculations (Table 5). This is attributed to the presence of oxide scale, which blocks inward diffusion of oxygen. Consequently, oxygen potential in the oxide scale, especially when it is dense, is much lower than in gas phase. Therefore, formed Si-rich phase is shifted from SiO_2 to Fe_2SiO_4 in steam (Figs. 4b, 5, 7, 10, 11 and 15) and from Fe_2SiO_4 to SiO_2 in H_2O–H_2 mixtures. With increasing oxidation time,

oxygen potential in the oxide scale will reach equilibrium with steam, further oxidizing metastable Fe_2SiO_4 into SiO_2 (Figs. 12 and 14).

4.3. Fe_2SiO_4 accumulation in spinel-type scale

Fe_2SiO_4 phase is non-uniformly distributed in spinel-type scale especially at temperatures ≥ 1200 ºC. The region near the spinel-spinel interface contains almost no Fe_2SiO_4 phase but lots of pores (Figs. 10 and 11). Two possible reasons may be responsible for this phenomenon. One is SiO_2 volatilization via the below reactions. Another is Fe_2SiO_4 inward movement upon oxidation.

$$SiO_2(s) + 2H_2O(g) = Si(OH)_4(g)\ \Delta G^o = 56733.0 + 66.2T\,J\cdot mol^{-1}\cdot K^{-1}\ [47]\ (3)$$

$$SiO_2(s) + H_2(g) = SiO(g) + H_2O(g)\ \Delta G^o = 540463.5 - 191.8T\,J\cdot mol^{-1}\cdot K^{-1}\ [46]\ (4)$$

SiO_2 interacts with steam at high temperatures, forming a range of Si hydroxide gaseous species [12]. $Si(OH)_4$ has been suggested as the dominant specie at temperatures above 800 ºC [12,47]. To evaluate SiO_2 volatilization via the above two reactions, $Si(OH)_4$ and SiO equilibrium pressures were plotted in Fig. 18 as a function of temperature. As seen, both $Si(OH)_4$ and SiO equilibrium pressures are extremely low in the present steam atmosphere, i.e., P_{H_2O} = 0.21 atm and f_{H_2}< 1.8 vol.% (averaged based on weight change of 304SS oxidized at 1200 ºC for 90 min), suggesting negligible SiO_2 volatilization. Cheng et al. [11] experimentally measured SiO_2 volatilization rate in steam atmosphere. According to their studies, relative weight loss of SiO_2 at 1200 ºC for 90 min in 0.84 atm steam is 4.9×10^{-4} %. SiO_2 volatilization rate linearly increases with steam pressure [11]. Therefore, in the present experimental condition of 0.21 atm steam, the relative weight loss of SiO_2 at 1200 ºC for 90 min is lower than 4.9×10^{-4} %. This value is too small to explain the large Fe_2SiO_4-poor region, which accounts for around 1/3 of the oxide scale in thickness. Furthermore, if SiO_2 volatilization occurred, Fe_2SiO_4 should be oxidized into SiO_2 first. SiO_2, however, was not observed in the Fe_2SiO_4-poor region near the spinel-spinel interface. Therefore, formation of the Fe_2SiO_4-poor region cannot be explained by SiO_2 volatilization under the present experimental conditions. Note that significant SiO_2 volatilization may occur during core degradation considering the extremely high steam pressure (>70 atm) in a boiling water reactor (BWR).

To prove that Fe_2SiO_4 phase moved inward during oxidation, we quantitatively characterized Si distribution in the oxide scale on 304SS oxidized in steam at 1200 ºC for 90 min. The inner oxide scale was equally divided into sub-regions as shown in Fig. 19a. Chemical composition of each sub-region was obtained using EPMA with the focused beam in scanning mode. The outermost region has the lowest Si content around 0.4 wt.%, which is much lower than initial Si content in 304SS.

The highest Si content appears in the middle region, where Si content is above 4.0 wt.%. According to the ratio of Cr content in the oxide scale to that in the metal matrix, average Si content in the oxide scale should be around 1.3 wt.%. Therefore, Si content profile in the inner oxide scale clearly indicates that Fe_2SiO_4 inward movement occurred during oxidation. Thermodynamically, Fe_2SiO_4 phase in the oxide scale is metastable (Fig. 17) and will be oxidized into SiO_2 when oxygen potential in the oxide scale exceeds a critical value. At the oxidation interface where oxygen potential is high enough to oxidize Fe_2SiO_4 phase, Fe_2SiO_4 phase is partly oxidized, with Fe entering surrounding $(Fe,Cr)_3O_4$ spinel phase and SiO_2 staying in Fe_2SiO_4 phase. Therefore, SiO_2 content becomes locally high and diffuses inward through Fe_2SiO_4 phase to react with Fe which diffuses outward, forming new Fe_2SiO_4 phase. Clearly, Fe_2SiO_4 inward movement results from Fe_2SiO_4 oxidation and re-formation. The underlying mechanism is schematically represented in Fig. 20. The melting point of Fe_2SiO_4 phase is 1205 ºC [48]. Therefore, Fe_2SiO_4 phase at 1200 ºC and 1300 ºC is in semi-liquid and liquid state, respectively. This guarantees rapid Si diffusion in Fe_2SiO_4 phase and thus rapid inward movement of Fe_2SiO_4 phase.

Several factors, such as presence of oxide scale, oxide scale spallation, and delayed SiO_2 formation in the spinel-type scale, may disadvantage SiO_2 volatilization. Therefore, the amount of Cs-bearing microparticles formed via SiO_2 volatilization and deposition may be limited during solid-state oxidation of 304SS at temperatures below 1250 ºC. Therefore, further studies on the oxidation of 304SS–B_4C melt, formed due to eutectic reaction in control rods, at higher temperatures are necessary.

5. Conclusions

In this work we studied Si distribution in the oxide scale on 304SS oxidized in H_2O–H_2 mixtures in the temperature range 1000–1300 ºC. Si-rich phase types and their distributions depend on the oxide scales formed on 304SS. Low temperatures (< 1200 ºC) and high H_2 contents in steam favour the formation of dense Cr_2O_3-type scale. On the contrary, high temperatures and low H_2 contents favour the formation of porous spinel-type scale. SiO_2 phase as a non-continuous film stays at the base of the Cr_2O_3-type scale. Fe_2SiO_2 phase is non-uniformly distributed in the spinel-type scale. More specifically, liquid Fe_2SiO_4 phase moved toward the metal-oxide interface during oxidation. This phenomenon was attributed to its thermodynamically metastable state in H_2O–H_2 mixtures. With increasing oxidation time, Fe_2SiO_2 phase was further oxidized into SiO_2 phase. Si distribution data obtained in this work could be coupled in the modelling of SiO_2 volatilization from 304SS.

Acknowledgement

The authors thank the International Research Institute for Nuclear Decommissioning (IRID) in Japan for financial support. The authors also thank Dr. M. Osaka in Japan Atomic Energy Agency (JAEA) for providing 304SS samples.

Data availability statement

The authors confirm that the data supporting the findings of this study are available within the article.

References

[1] A.L. Nichols, D.L. Aldama, M. Verpelli, Handbook of nuclear data for safeguards: database extensions, August 2008, IAEA, Vienna, 2008.

[2] N. Kaneyasu, H. Ohashi, F. Suzuki, T. Okuda, F. Ikemori, Sulfate aerosol as a potential transport medium of radiocesium from the fukushima nuclear accident, Environ. Sci. Technol. 46 (2012) 5720–5726. doi:10.1021/es204667h.

[3] K. Adachi, M. Kajino, Y. Zaizen, Y. Igarashi, Emission of spherical cesium-bearing particles from an early stage of the Fukushima nuclear accident., Sci. Rep. 3 (2013) 2554. doi:10.1038/srep02554.

[4] Y. Abe, Y. Iizawa, Y. Terada, K. Adachi, Y. Igarashi, I. Nakai, Detection of uranium and chemical state analysis of individual radioactive microparticles emitted from the Fukushima nuclear accident using multiple synchrotron radiation X-ray analyses, Anal. Chem. 86 (2014) 8521–8525. doi:10.1021/ac501998d.

[5] T. Kogure, N. Yamaguchi, H. Segawa, H. Mukai, S. Motai, K. Akiyama-Hasegawa, M. Mitome, T. Hara, T. Yaita, Constituent elements and their distribution in the radioactive Cs-bearing silicate glass microparticles released from Fukushima nuclear plant, Microscopy. 65 (2016) 451–459. doi:10.1093/jmicro/dfw030.

[6] N. Yamaguchi, M. Mitome, A.-H. Kotone, M. Asano, K. Adachi, T. Kogure, Internal structure of cesium-bearing radioactive microparticles released from Fukushima nuclear power plant., Sci. Rep. 6 (2016) 20548. doi:10.1038/srep20548.

[7] Y. Satou, K. Sueki, K. Sasa, K. Adachi, Y. Igarashi, First successful isolation of radioactive particles from soil near the Fukushima Daiichi Nuclear Power Plant, Anthropocene. 14 (2016) 71–76. doi:10.1016/j.ancene.2016.05.001.

[8] N. Yamaguchi, T. Kogure, H. Mukai, K. Akiyama-Hasegawa, M. Mitome, T. Hara, H. Fujiwara, Structures of radioactive Cs-bearing microparticles in non-spherical forms collected in Fukushima, Geochem. J. 51 (2017). doi:10.2343/geochemj.2.0483.

[9] S. Higaki, Y. Kurihara, H. Yoshida, Y. Takahashi, N. Shinohara, Discovery of non-spherical heterogeneous radiocesium-bearing particles not derived from Unit 1 of the Fukushima Dai-ichi Nuclear Power Plant, in residences five years after the accident, J. Environ. Radioact. 177 (2017) 65–70. doi:10.1016/j.jenvrad.2017.06.006.

[10] T. Ogawa, T. Do, S. Sujatanond, T. Ogitsu, H. Shiwaku, M. Nakada, M. Akabori, Interpreting radioactive microspheres released in Fukushima Daiichi Nuclear Plant accident

in view of XANES and thermodynamic database, presentation given in 250th ACS National Meeting, Boston, 16-20 August, 2015.

[11] M.-C. Cheng, I.B. Cutler, Vaporization of silica in steam atmosphere, J. Am. Ceram. Soc. 62 (1979) 593–596. doi:10.1111/j.1151-2916.1979.tb12739.x.

[12] N.S. Jacobson, E.J. Opila, D.L. Myers, E.H. Copland, Thermodynamics of gas phase species in the Si-O-H system, J. Chem. Thermodyn. 37 (2005) 1130–1137. doi:10.1016/j.jct.2005.02.001.

[13] S. Elhadj, M.J. Matthews, S.T. Yang, D.J. Cooke, Evaporation kinetics of laser heated silica in reactive and inert gases based on near-equilibrium dynamics, Opt. Express. 20 (2012) 1575–1587. doi:10.1364/OE.20.001575.

[14] A. Itoh, Cesium chemistry model in SAMPSON code, presentation given in CLADS workshop, Tomioka, 5-6 July, 2017.

[15] A. Suzuki, Simulation study on Cs-bearing particle formation: vaporization and deposition, presentation given in CLADS workshop, Tomioka, 5-6 July, 2017.

[16] H.E. Evans, D.A. Hilton, R.A. Holm, S.J. Webster, Influence of silicon additions on the oxidation resistance of a stainless steel, Oxid. Met. 19 (1983) 1–18. doi:10.1007/BF00656225.

[17] J. Robertson, M.I. Manning, Healing layer formation in Fe–Cr–Si ferritic steels, Mater. Sci. Technol. 5 (1989) 741–753. doi:10.1179/mst.1989.5.8.741.

[18] S.N. Basu, G.J. Yurek, Effect of alloy grain size and silicon content on the oxidation of austenitic Fe-Cr-Ni-Mn-Si alloys in pure O_2, Oxid. Met. 36 (1991) 281–315. doi:10.1007/BF00662967.

[19] J.S. Dunning, D.E. Alman, J.C. Rawers, Influence of silicon and aluminum additions on the oxidation resistance of a lean-chromium stainless steel, Oxid. Met. 57 (2002) 409–425. doi:10.1023/A:1015344220073.

[20] A.M. Huntz, V. Bague, G. Beauplé, C. Haut, C. Sévérac, P. Lecour, X. Longaygue, F. Ropital, Effect of silicon on the oxidation resistance of 9% Cr steels, Appl. Surf. Sci. 207 (2003) 255–275. doi:10.1016/S0169-4332(02)01505-2.

[21] T. Ishitsuka, Y. Inoue, H. Ogawa, Effect of silicon on the steam oxidation resistance of a 9% Cr heat-resistant steel, Oxid. Met. 61 (2004) 125–142.

[22] B. Li, B. Gleeson, Effects of silicon on the oxidation behavior of Ni-base chromia-forming alloys, Oxid. Met. 65 (2006) 101–122. doi:10.1007/s11085-006-9003-4.

[23] G. Bamba, Y. Wouters, A. Galerie, F. Charlot, A. Dellali, Thermal oxidation kinetics and oxide scale adhesion of Fe-15Cr alloys as a function of their silicon content, Acta Mater. 54 (2006) 3917–3922. doi:10.1016/j.actamat.2006.04.023.

[24] A. Paúl, R. Sánchez, O.M. Montes, J.A. Odriozola, The role of silicon in the reactive-elements effect on the oxidation of conventional austenitic stainless steel, Oxid. Met. 67 (2007) 87–105. doi:10.1007/s11085-006-9046-6.

[25] Y. Liu, W. Wei, L. Benum, M. Oballa, M. Gyorffy, W. Chen, Oxidation behavior of Ni-Cr-Fe-based alloys: Effect of alloy microstructure and silicon content, Oxid. Met. 73 (2010) 207–218. doi:10.1007/s11085-009-9172-z.

[26] A.A. Mouayd, A. Koltsov, E. Sutter, B. Tribollet, Effect of silicon content in steel and oxidation temperature on scale growth and morphology, Mater. Chem. Phys. 143 (2014)

996–1004. doi:10.1016/j.matchemphys.2013.10.037.

[27] A.M. Huntz, A. Reckmann, C. Haut, C. Sévérac, M. Herbst, F.C.T. Resende, A.C.S. Sabioni, Oxidation of AISI 304 and AISI 439 stainless steels, Mater. Sci. Eng. A. 447 (2007) 266–276. doi:10.1016/j.msea.2006.10.022.

[28] N. Karimi, F. Riffard, F. Rabaste, S. Perrier, R. Cueff, C. Issartel, H. Buscail, Characterization of the oxides formed at 1000 °C on the AISI 304 stainless steel by X-ray diffraction and infrared spectroscopy, Appl. Surf. Sci. 254 (2008) 2292–2299. doi:10.1016/j.apsusc.2007.09.018.

[29] G.J. Yurek, D. Eisen, A. Garratt-Reed, Oxidation behavior of a fine-grained rapidly solidified 18-8 stainless steel, Metall. Trans. A. 13 (1982) 473–485. doi:10.1007/BF02643355.

[30] M. Arshed, M. Siddique, M. Anwar-ul-Islam, N. Hussain, K.A. Shahid, N.M. Butt, Study of oxidation of alloy 1.4306S (SS-304L) in air and steam at 1200°C using the Mössbauer technique, J. Radioanal. Nucl. Chem. 224 (1997) 3–6. doi:10.1007/BF02034603.

[31] N. Materials, N.S. Engineering, T. I-chome, Oxidation of 304 stainless steel in high-temperature steam, J. Nucl. Mater. 140 (1986) 74–84.

[32] J.T. Bittel, L.H. Sjodahl, J.F. White, Oxidation of 304L stainless steel by steam and by air, Corrosion. 25 (1969) 7–14. doi:10.5006/0010-9312-25.1.7.

[33] M. Steinbrück, Degradation and oxidation of B_4C control rod segments at high temperatures, J. Nucl. Mater. 400 (2010) 138–150. doi:10.1016/j.jnucmat.2010.02.022.

[34] P. Deines, R.H. Nafziger, G.C. Ulmer, E. Woermann, Temperature-oxygen fugacity tables for selected gas mixtures in the system C-H-O at one atmosphere total pressure, Bull. Earth Miner. Sci. Exp. Sta. Pennsylvania State Univ. 88 (1974) 1–129.

[35] R. Bauer, M. Baccalaro, L.P.H. Jeurgens, M. Pohl, E.J. Mittemeijer, Oxidation behavior of Fe-25Cr-20Ni-2.8Si during isothermal oxidation at 1,286 K; Life-time prediction, Oxid. Met. 69 (2008) 265–285. doi:10.1007/s11085-008-9097-y.

[36] F.H. Stott, G.C. Wood, J. Stringer, The influence of alloying elements on the development and maintenance of protective scales, Oxid. Met. 44 (1995) 113–145. doi:10.1007/BF01046725.

[37] A.M. Emsley, M.P. Hill, Intergranular oxidation of silicon in 20Cr-25Ni niobium-stabilized stainless steel at 1140-1230 K, Oxid. Met. 34 (1990) 351–360. doi:10.1007/BF00665023.

[38] F.J. Pérez, E. Otero, M.P. Hierro, C. Gómez, F. Pedraza, J.L. de Segovia, E. Román, High temperature corrosion protection of austenitic AISI 304 stainless steel by Si, Mo and Ce ion implantation, Surf. Coatings Technol. 108–109 (1998) 127–131. doi:10.1016/S0257-8972(98)00685-9.

[39] P.J. Potts, A handbook of silicate rock analysis, 2nd ed., Springer Science & Business Media, NewYork, 1992. doi:10.1007/978-94-015-3988-3_10.

[40] H.E. Evans, A.T. Donaldson, Silicon and chromium depletion during the long-term oxidation of thin-sectioned austenitic steel, Oxid. Met. 50 (1998) 457–475. doi:10.1023/A:1018808925756.

[41] G. Eriksson, P. Wu, M. Blander, A.D. Pelton, Critical evaluation and optimization of the thermodynamic properties and phase diagrams of the $MnO–SiO_2$ and $CaO–SiO_2$ systems, Can. Metall. Q. 33 (1994) 13–21. doi:10.1179/cmq.1994.33.1.13.

[42] N. Birks, G.H. Meier, F.S. Pettit, Introduction to the high-temperature oxidation of metals, Second, Cambridge University Press, Cambridge, 2006.

[43] D.W. Yun, S.M. Seo, H.W. Jeong, Y.S. Yoo, The effects of the minor alloying elements Al, Si and Mn on the cyclic oxidation of Ni-Cr-W-Mo alloys, Corros. Sci. 83 (2014) 176–188. doi:10.1016/j.corsci.2014.02.015.

[44] J.-H. Kim, D.-I. Kim, S. Suwas, E. Fleury, K.-W. Yi, Grain-size effects on the high-temperature oxidation of modified 304 austenitic stainless steel, Oxid. Met. 79 (2013) 239–247. doi:10.1007/s11085-012-9347-x.

[45] X. Ren, K. Sridharan, T.R. Allen, Effect of grain refinement on corrosion of ferritic-martensitic steels in supercritical water environment, Mater. Corros. 61 (2010) 748–755. doi:10.1002/maco.200905446.

[46] I. Barin, Thermochemical data of pure substances, 3rd ed., VCH Verlagsgesellschaft mbH, Weinheim, 1995. doi:10.1002/9783527619825.

[47] A. Hashimoto, The effect of H_2O gas on volatilities of planet-forming major elements: I. Experimental determination of thermodynamic properties of Ca-, Al-, and Si-hydroxide gas molecules and its application to the solar nebula, Geochim. Cosmochim. Acta. 56 (1992) 511–532.

[48] W.E. Jackson, J. Mustre de Leon, G.E. Brown Jr., G.A. Waychunas, S.D. Conradson, J.-M. Combes, High-temperature XAS study of Fe_2SiO_4 liquid: Reduced coordination of ferrous iron, Science. 262 (1993) 229–233. doi:10.1126/science.262.5131.229.

Figure Captions

Fig. 1 Relative weight change of 304SS exposed in CO_2 atmosphere under transient condition.

Fig. 2 Weight changes of 304SS isothermally oxidized in the temperature range 1000–1300 ºC.

Fig. 3 Weight change of 304SS as a function of time during isothermal oxidation at 1200 ºC.

Fig. 4 Microstructure of the oxide scale on 304SS oxidized in steam at 1000 ºC for 120 min. (a) Dense oxide scale; (b) Porous oxide scale; (c) Elemental mappings of the whole region shown in Fig. 4b.

Fig. 5 Microstructure of the porous oxide scale on 304SS oxidized in steam at 1150 ºC for 60 min.

Fig. 6 Microstructure of the dense oxide scale on 304SS oxidized in steam at 12000 ºC for 60 min.

Fig. 7 Microstructure of the porous oxide scale on 304SS oxidized in steam at 12000 ºC for 60 min. (a) Overview of the oxide scale; (b) and (c) Enlarged views of the regions indicated by the rectangles; (d) Si mapping of the region indicated by the dashed-line rectangle in Fig. 7a.

Fig. 8 Chemical composition of the inner oxide scale versus distance from the metal-oxide interface for 304SS oxidized in steam at 1200 ºC for 60 min.

Fig. 9 Chemical composition of the metallic phase in the oxide scale versus distance from the metal-oxide interface for 304SS oxidized in steam at 1200 ºC for 60 min.

Fig. 10 Microstructure of the oxide scale on 304SS oxidized in steam at 1300 ºC for 60 min. (a) Overview of the oxide scale; (b) and (c) Enlarged views of the regions indicated by the rectangles; (d) and (e) Si and Ni mappings of the region indicated by the double sided arrow in Fig. 10a.

Fig. 11 Microstructure of the oxide scale on 304SS oxidized in steam at 1200 ºC for 90 min. (a) Overview of the oxide scale; (b), (c) and (d) Enlarged views of the regions indicated by the rectangles; (e) Si mapping of the whole region shown in Fig .11a.

Fig. 12 Microstructure of the oxide scale on 304SS oxidized in steam at 1200 ºC for 120 min. (a) Overview of the oxide scale; (b) Enlarged view of the region indicated by the rectangle; (c) Si mapping of the region shown in Fig. 12a.

Fig. 13 Microstructure of the oxide scale remained on the metal matrix of 304SS oxidized in steam at 1200 ºC for 120 min.

Fig. 14 Microstructure of the oxide scale on 304SS oxidized in steam at 1200 ºC for 180 min. (a) Overview of the oxide scale; (b) Enlarged view of the region indicated by the rectangle; (c) and (d) Cr and Si mappings of the rectangular region.

Fig. 15 Microstructure of the oxide scale on 304SS oxidized in 89% H_2O–11% H_2 at 1200 ºC for 60 min.

Fig. 16 Predominance diagram for Fe–Cr mixture in equilibrium with oxygen. Thermodynamic data is taken from Ref. [46].

Fig. 17 Predominance diagram for Fe-Si mixture in equilibrium with oxygen. Thermodynamic data is taken from Ref. [46].

Fig. 18 $Si(OH)_4$ and SiO equilibrium pressures as a function of temperature.

Fig. 19 Si and Cr content profiles across inner oxide scale on 304SS oxidized in steam at 1200 ºC for 90 min. (a) Micrograph; (b) Si and Cr content profiles.

Fig. 20 Schematic representation of Fe_2SiO_4 inward movement in the oxide scale upon oxidation.

Table Captions

Table 1 Chemical composition of 304SS investigated, wt.%.

Table 2 Details of the experimental conditions.

Table 3 Chemical compositions of the spots indicated by plus sign, at.%.

Table 4 Chemical composition of Si-rich phase averaged from 4 randomly selected spots in the inner oxide scale shown in Fig. 12, at.%.

Table 5 Summary of oxide scales and Si-rich phases in the oxide scale.

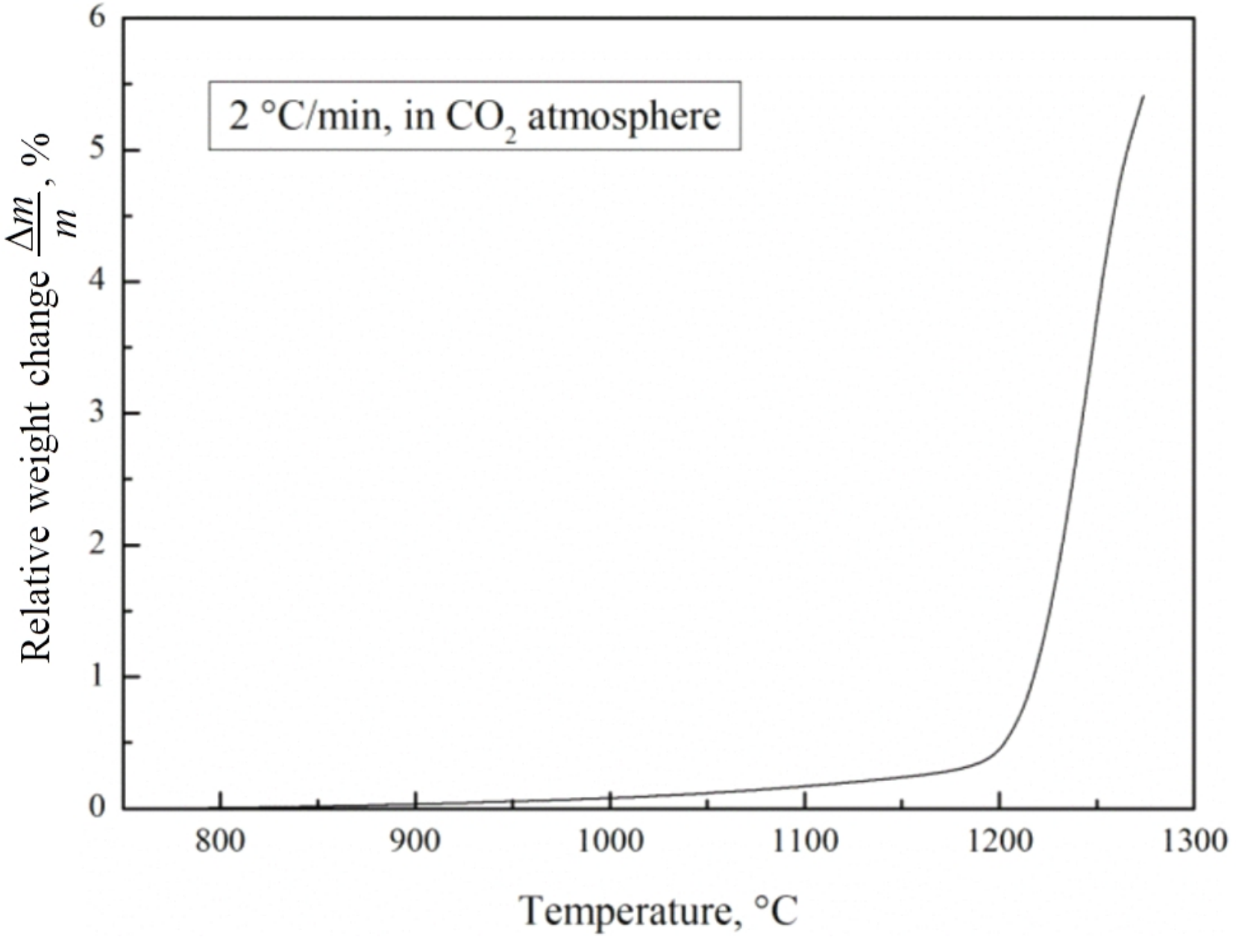
2 °C/min, in CO_2 atmosphere
Relative weight change $\frac{\Delta m}{m}$, %
Temperature, °C
0
1
2
3
4
5
6
800
900
1000
1100
1200
1300

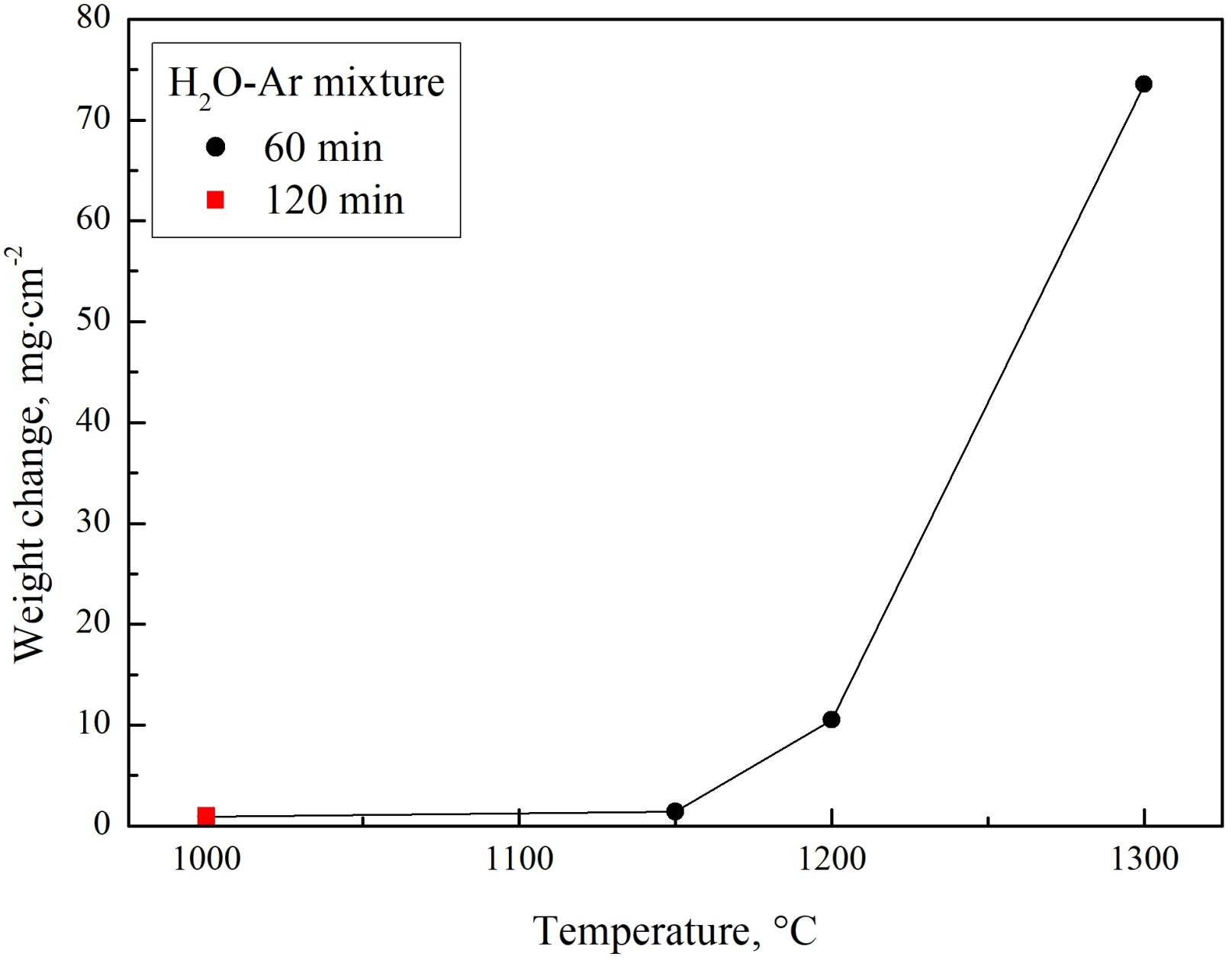
H2O-Ar mixture
60 min
120 min
Weight change, mg·cm-2
Temperature, °C
0
10
20
30
40
50
60
70
80
1000
1100
1200
1300

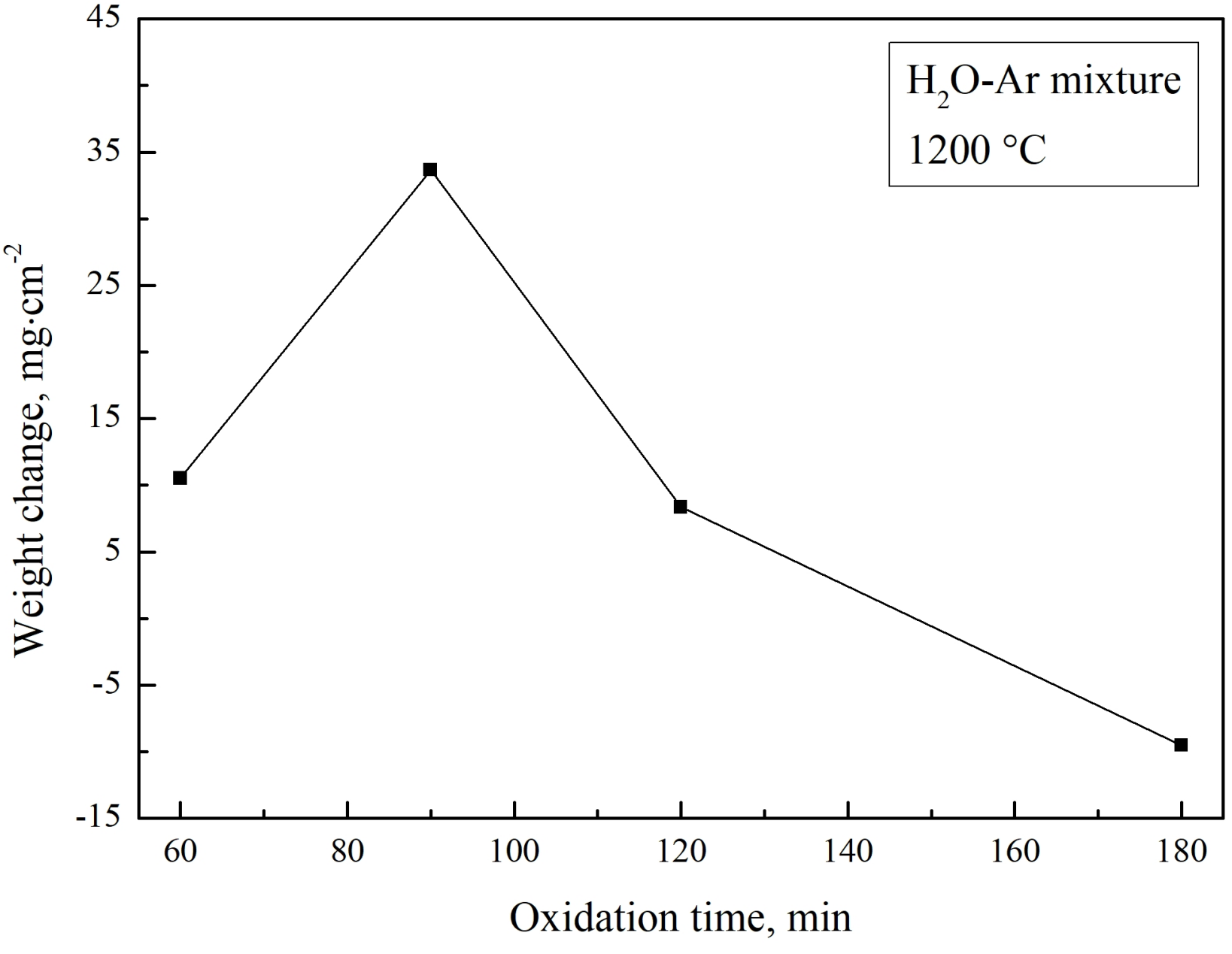
H2O-Ar mixture
1200 °C
Weight change, mg·cm-2
Oxidation time, min
45
35
25
15
5
-5
-15
60
80
100
120
140
160
180

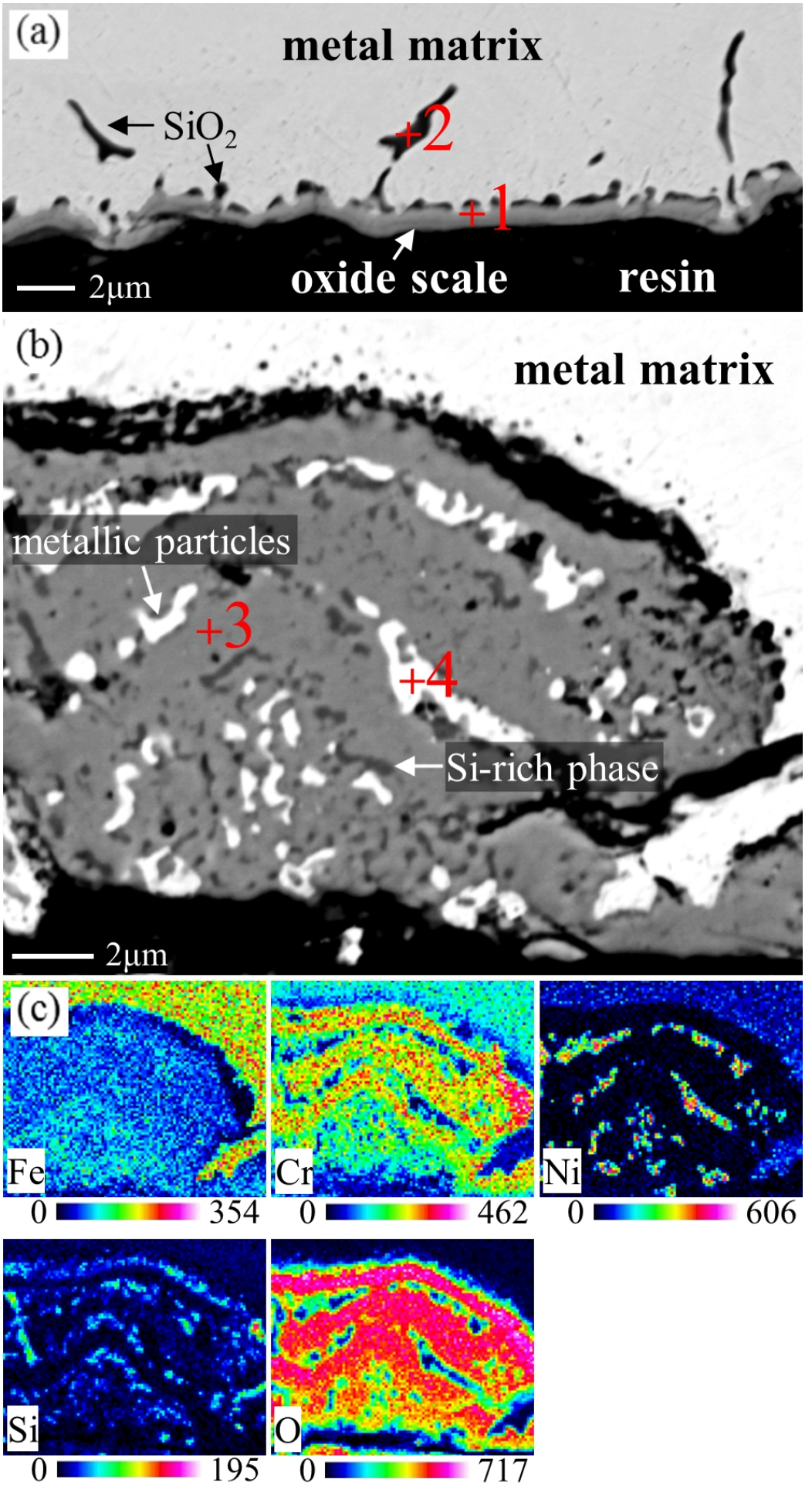
(a)
metal matrix
SiO2
+2
+1
oxide scale
resin
2μm
(b)
metal matrix
metallic particles
+3
+4
Si-rich phase
2μm
(c)
Fe
0
354
Cr
0
462
Ni
0
606
Si
0
195
O
0
717

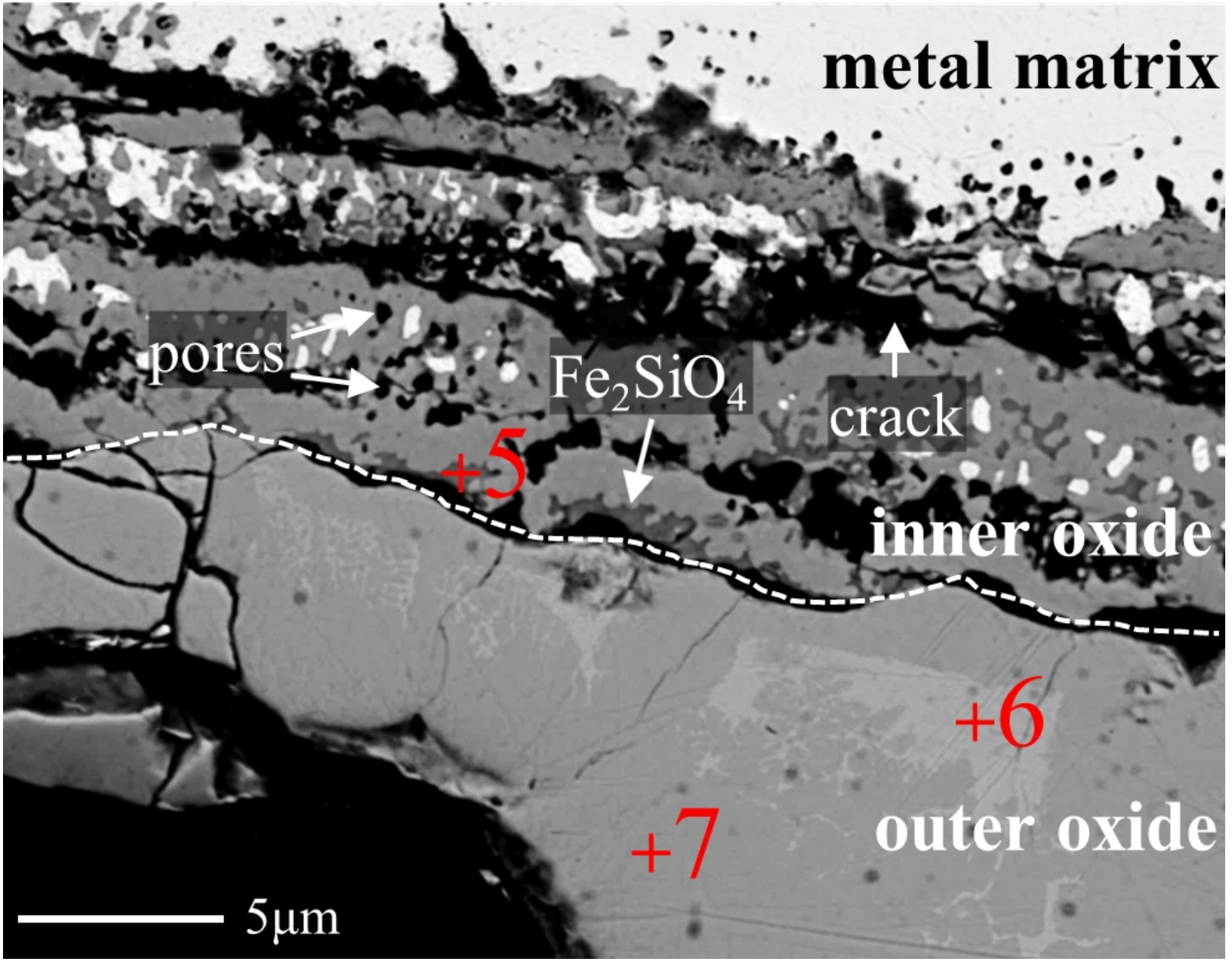
metal matrix
pores
Fe_2SiO_4
crack
+5
inner oxide
+6
+7
outer oxide
5μm

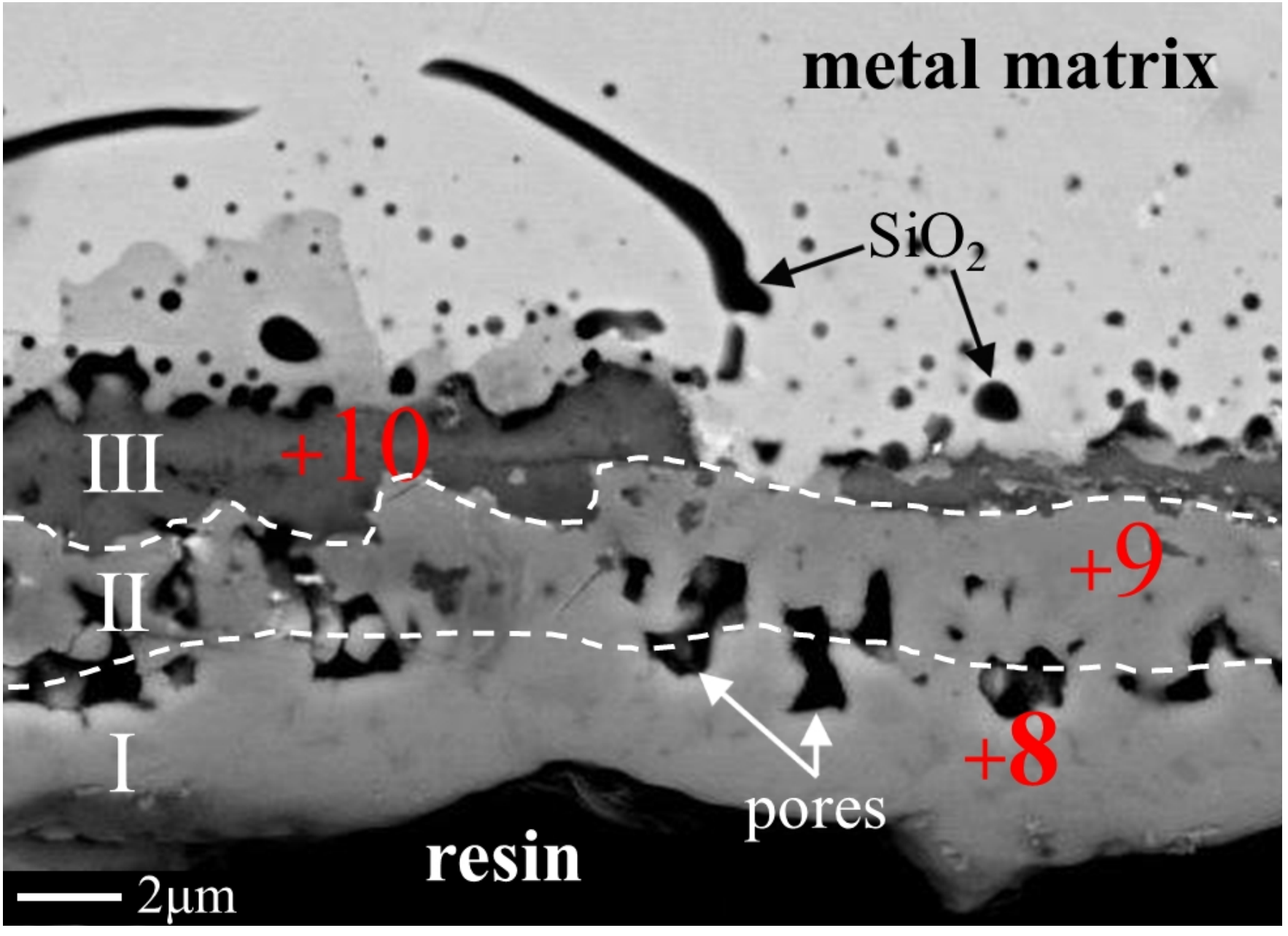
metal matrix
SiO_2
III
+10
II
+9
I
+8
pores
resin
2μm

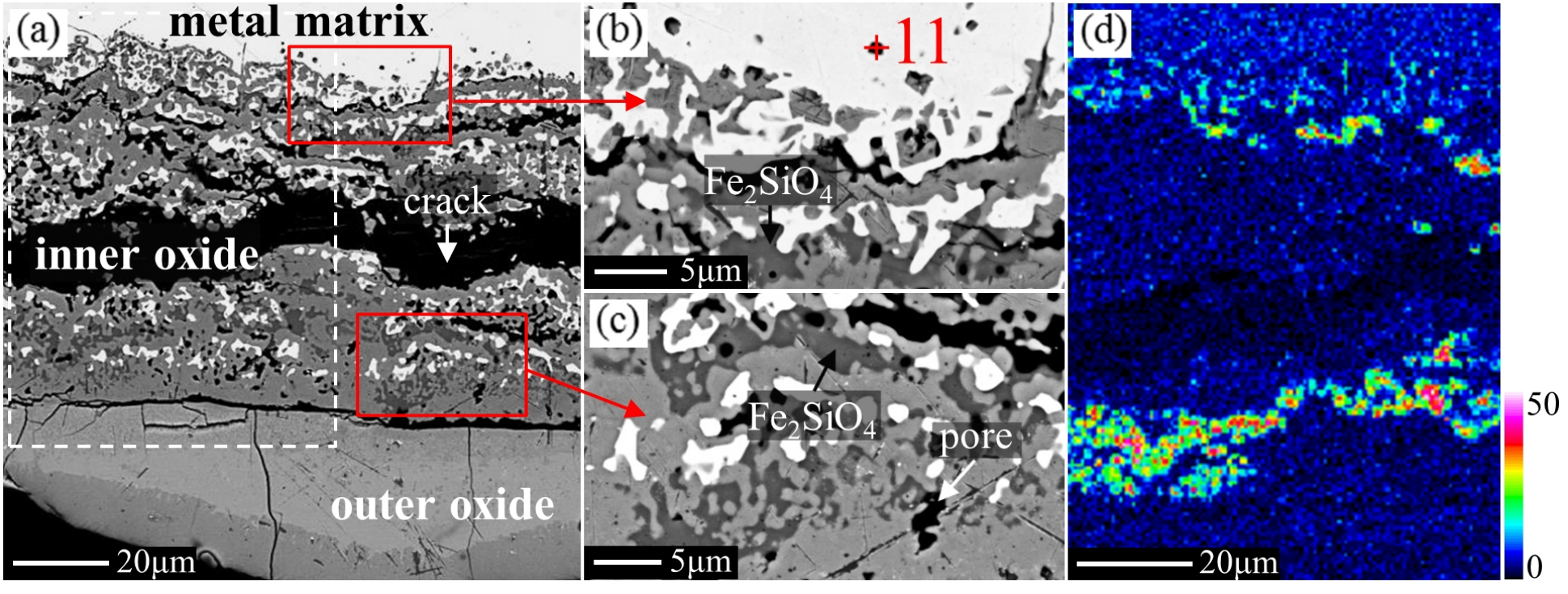
(a)
metal matrix
crack
inner oxide
outer oxide
20μm
(b)
+11
Fe_2SiO_4
5μm
(c)
Fe_2SiO_4
pore
5μm
(d)
20μm
50
0

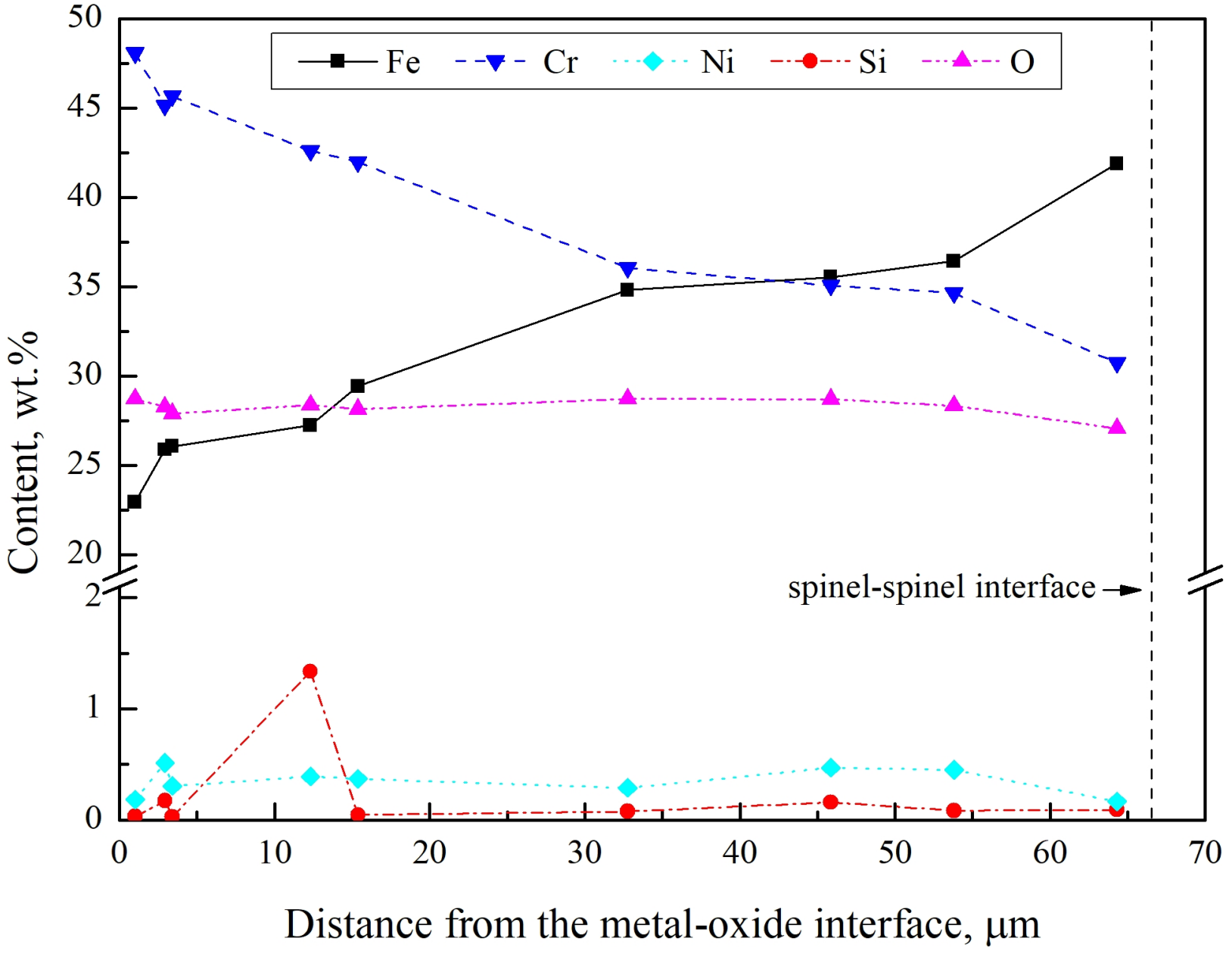
Fe
Cr
Ni
Si
O
spinel-spinel interface
Content, wt.%
Distance from the metal-oxide interface, μm
50
45
40
35
30
25
20
2
1
0
0
10
20
30
40
50
60
70

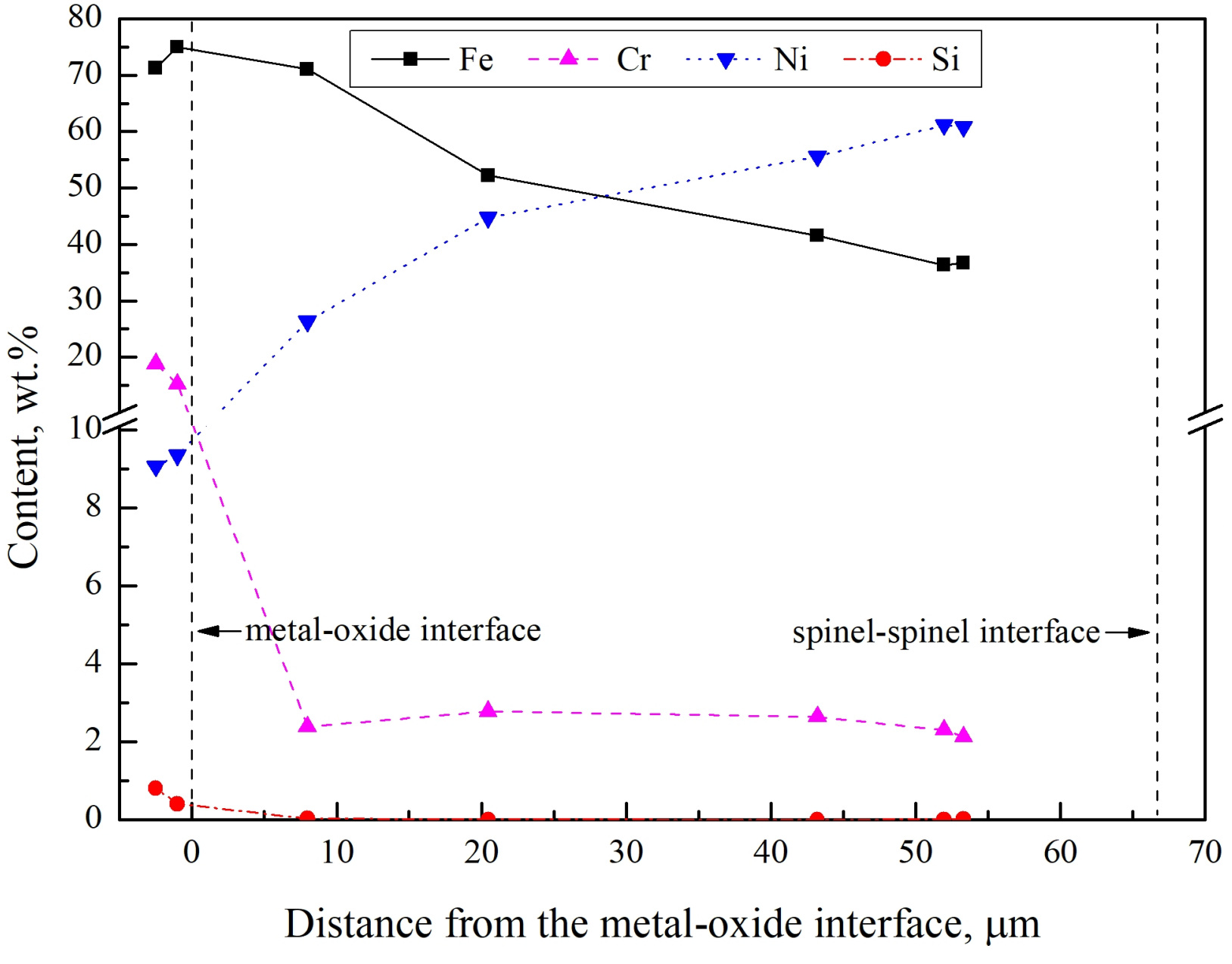
Fe
Cr
Ni
Si
metal-oxide interface
spinel-spinel interface
Content, wt.%
Distance from the metal-oxide interface, μm
80
70
60
50
40
30
20
10
8
6
4
2
0
0
10
20
30
40
50
60
70

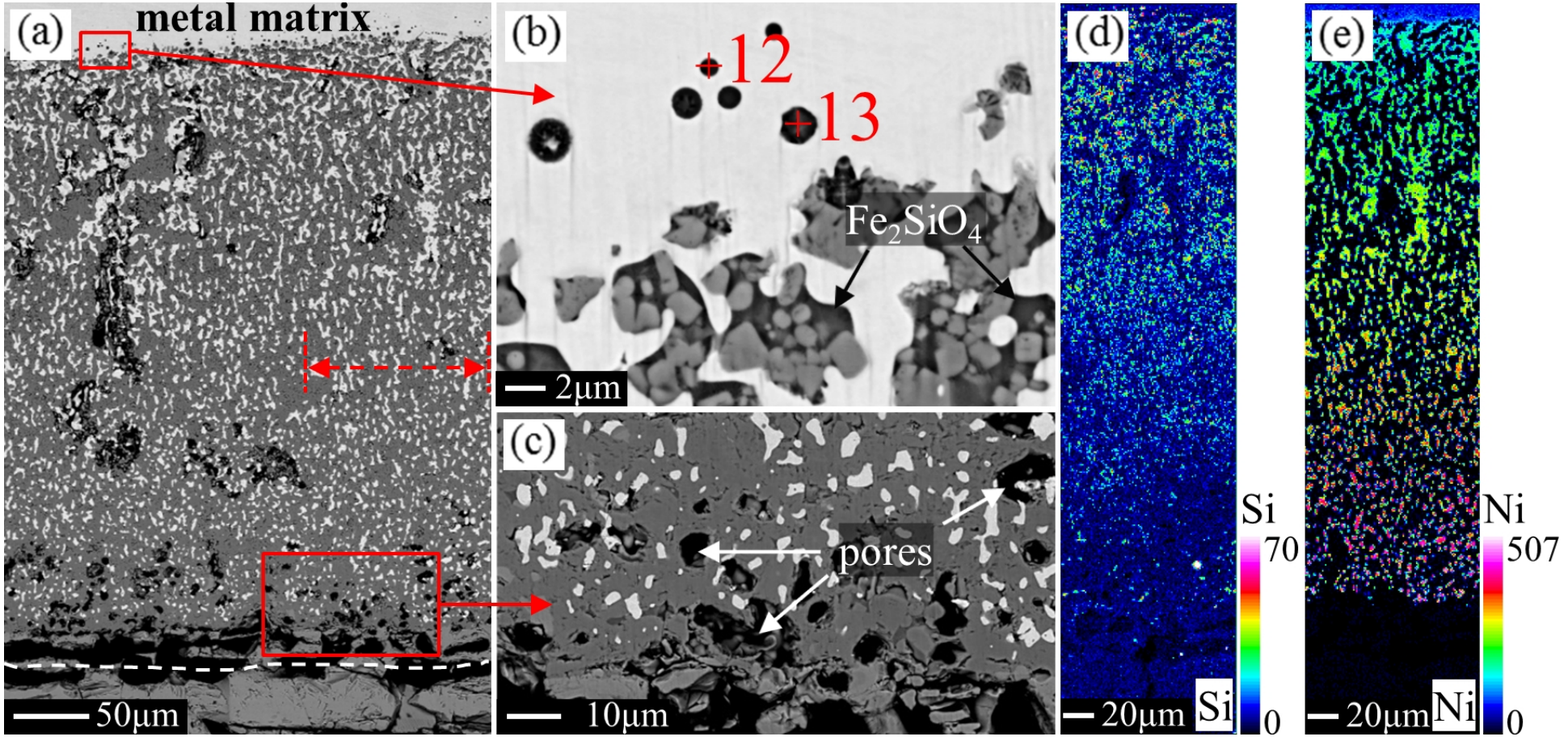
(a)
metal matrix
50μm
(b)
12
13
Fe_2SiO_4
2μm
(c)
pores
10μm
(d)
Si
20μm
Si
70
0
(e)
Ni
20μm
Ni
507
0

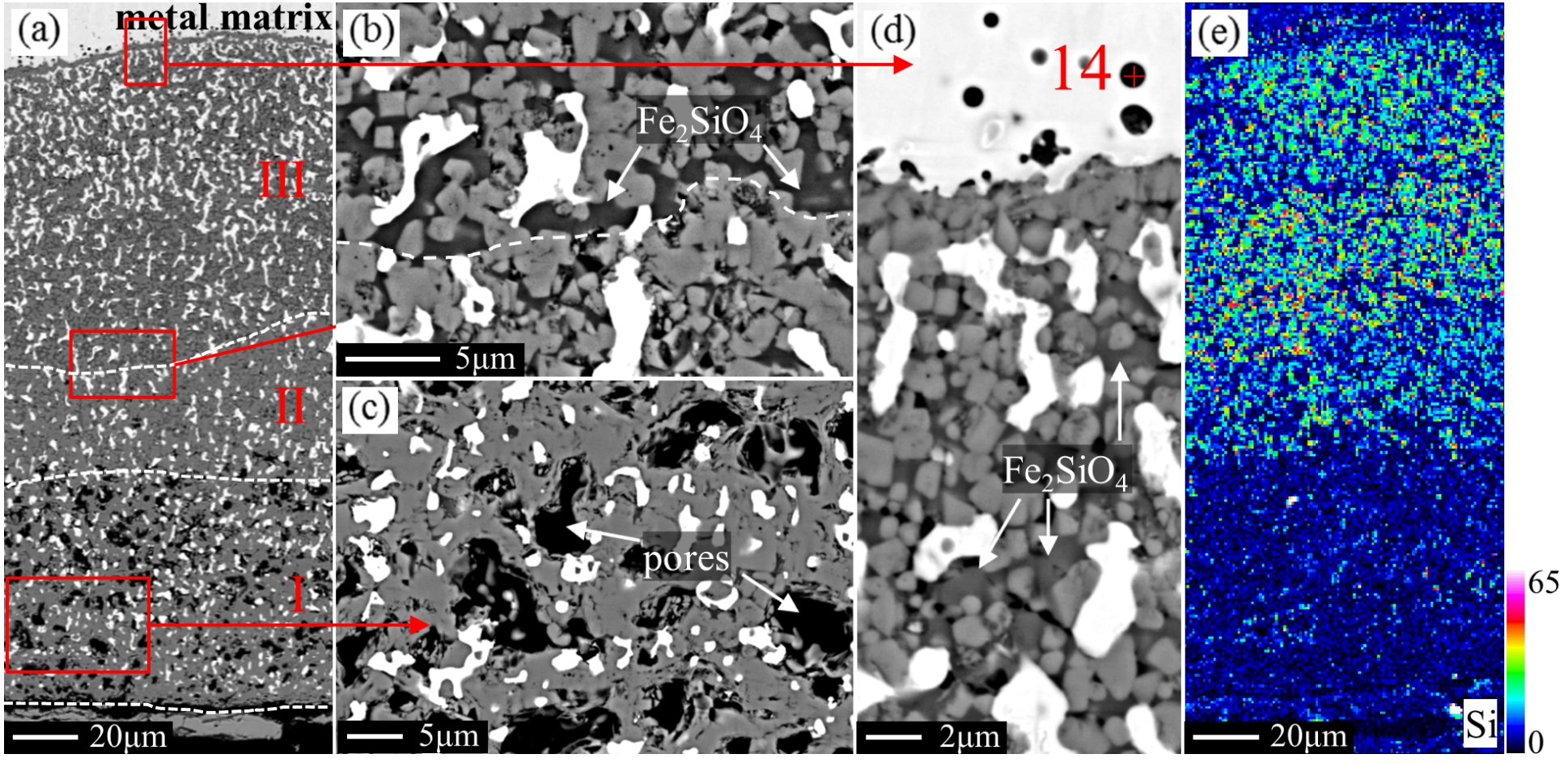
(a)
metal matrix
III
II
I
20μm
(b)
Fe2SiO4
5μm
(c)
pores
5μm
(d)
14
Fe2SiO4
2μm
(e)
20μm
Si
65
0

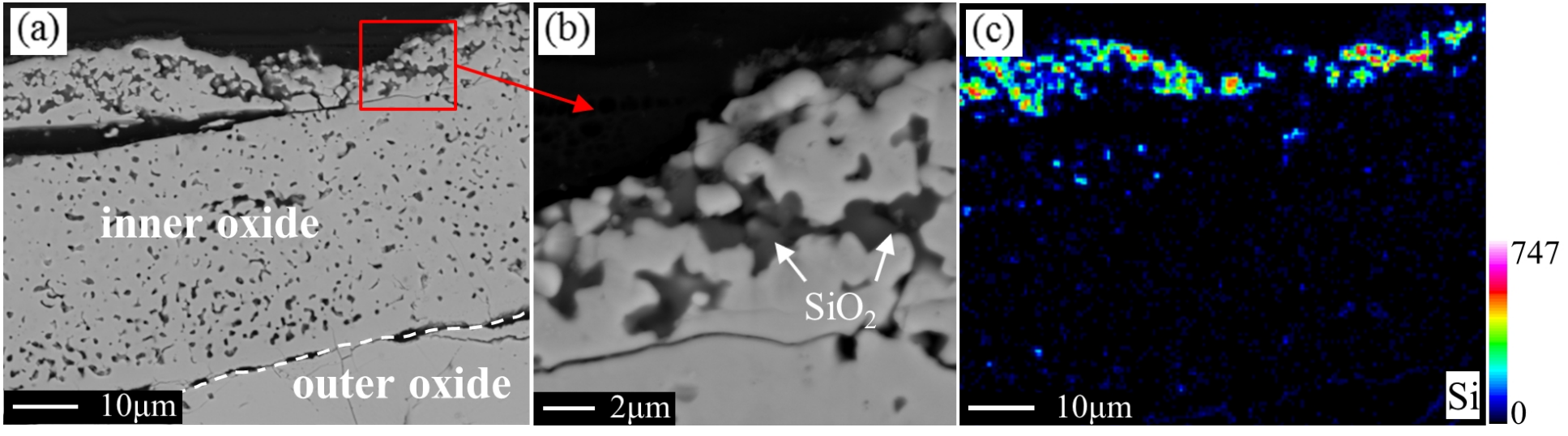
(a)
inner oxide
outer oxide
10μm
(b)
SiO2
2μm
(c)
10μm
Si
747
0

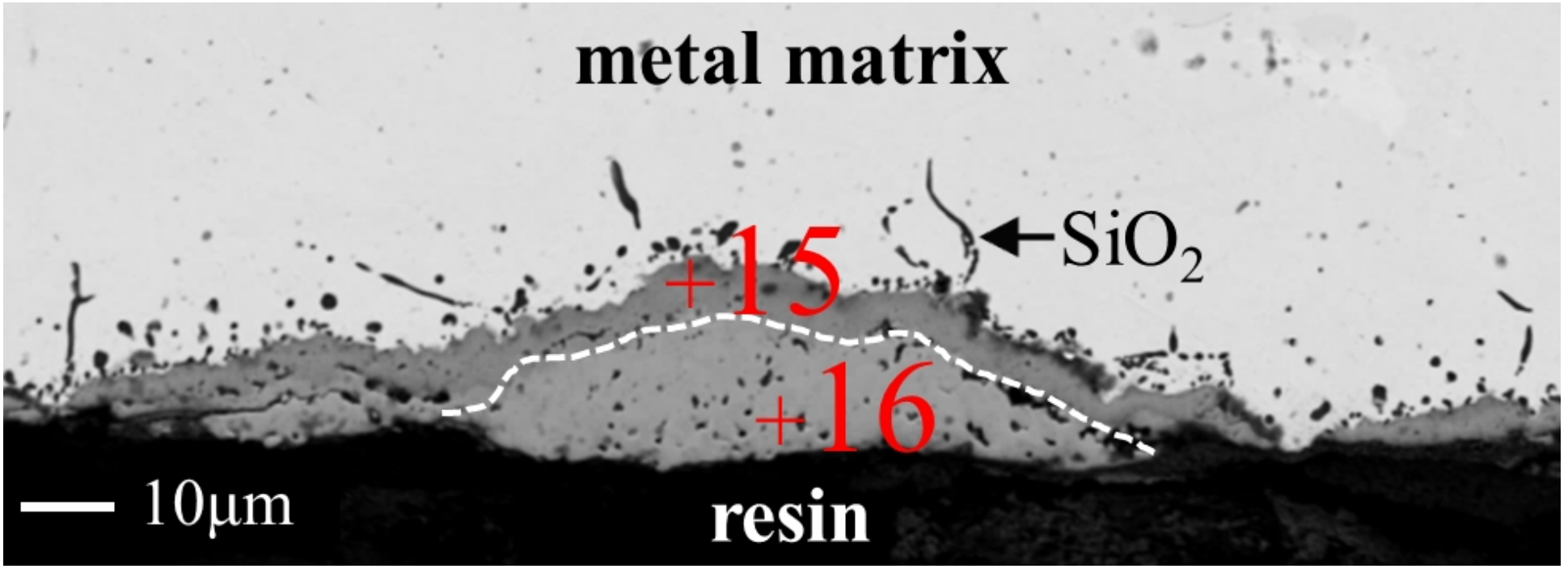
metal matrix
SiO2
+15
+16
10μm
resin

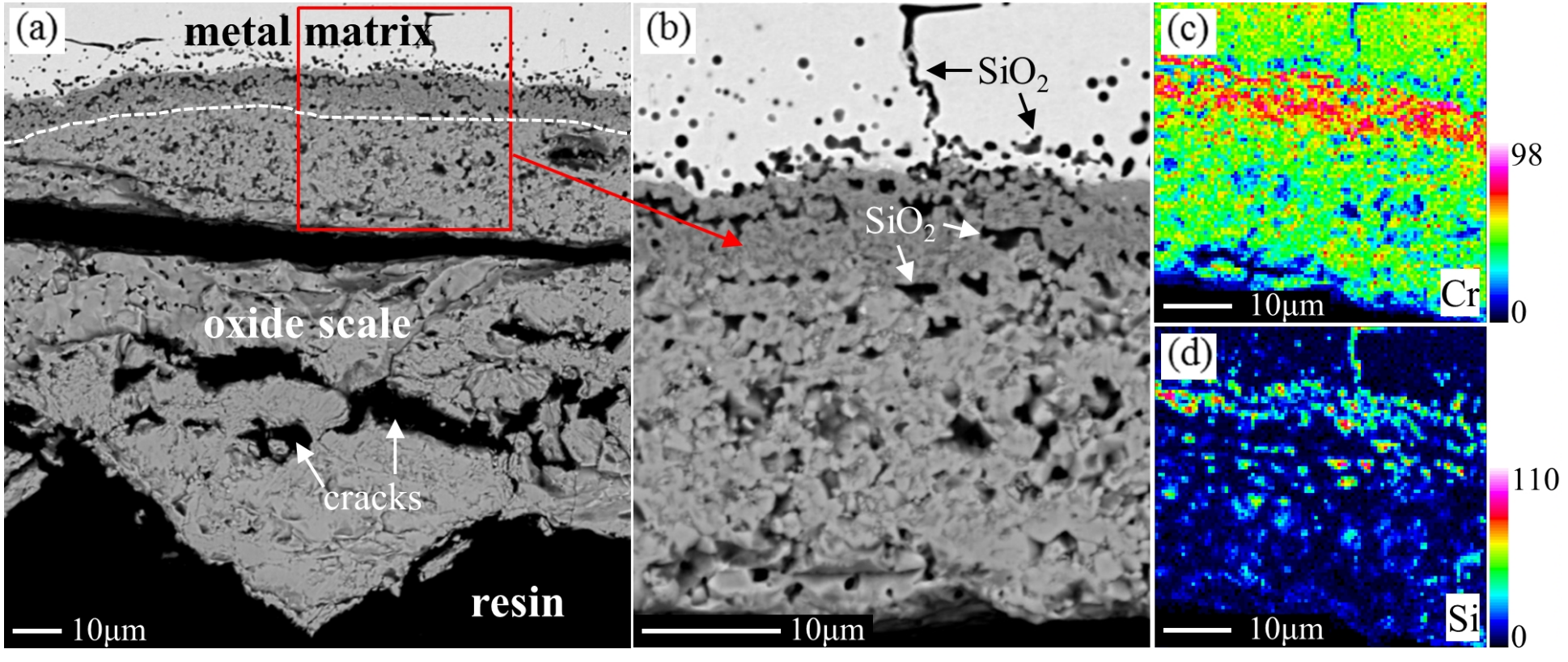
(a)
metal matrix
oxide scale
cracks
resin
10μm
(b)
SiO2
SiO2
10μm
(c)
98
0
10μm
Cr
(d)
110
0
10μm
Si

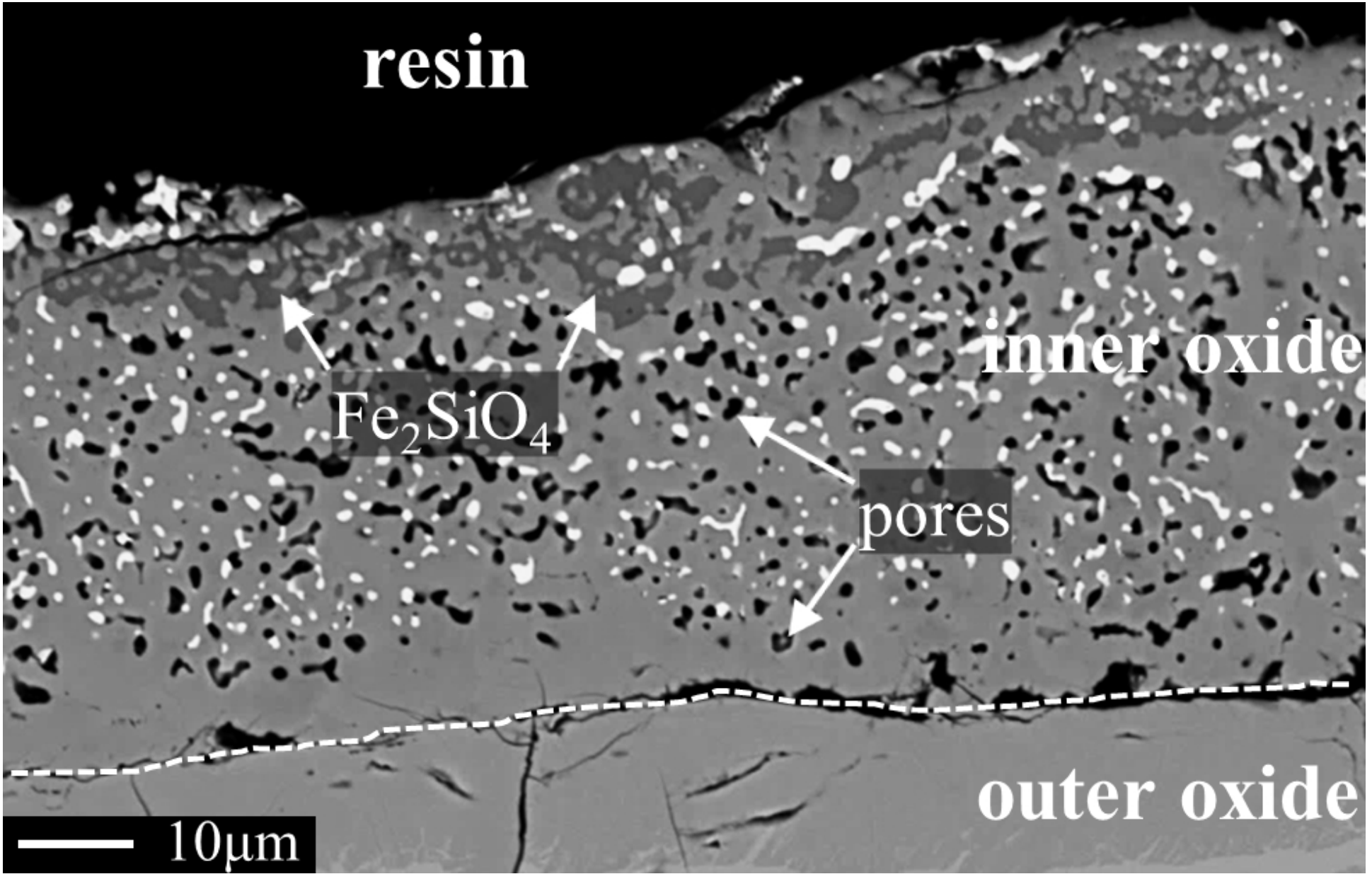
resin
inner oxide
Fe_2SiO_4
pores
outer oxide
10μm

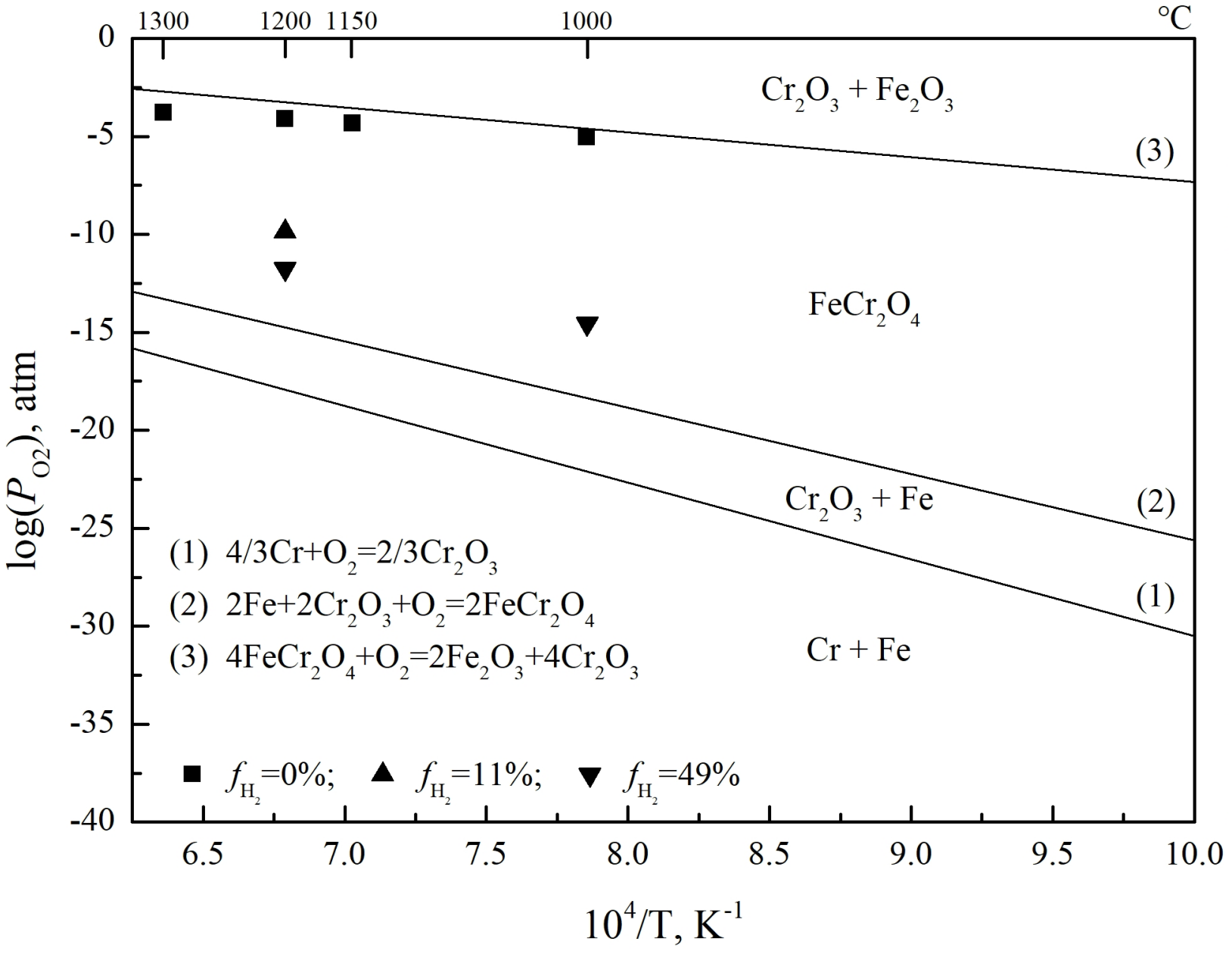
1300
1200
1150
1000
°C
0
-5
-10
-15
-20
-25
-30
-35
-40
log(P_{O2}), atm
$Cr_2O_3 + Fe_2O_3$
(3)
$FeCr_2O_4$
$Cr_2O_3 + Fe$
(2)
(1)
Cr + Fe
(1) $4/3Cr+O_2=2/3Cr_2O_3$
(2) $2Fe+2Cr_2O_3+O_2=2FeCr_2O_4$
(3) $4FeCr_2O_4+O_2=2Fe_2O_3+4Cr_2O_3$
f_{H_2}=0%; f_{H_2}=11%; f_{H_2}=49%
6.5
7.0
7.5
8.0
8.5
9.0
9.5
10.0
$10^4/T$, K^{-1}

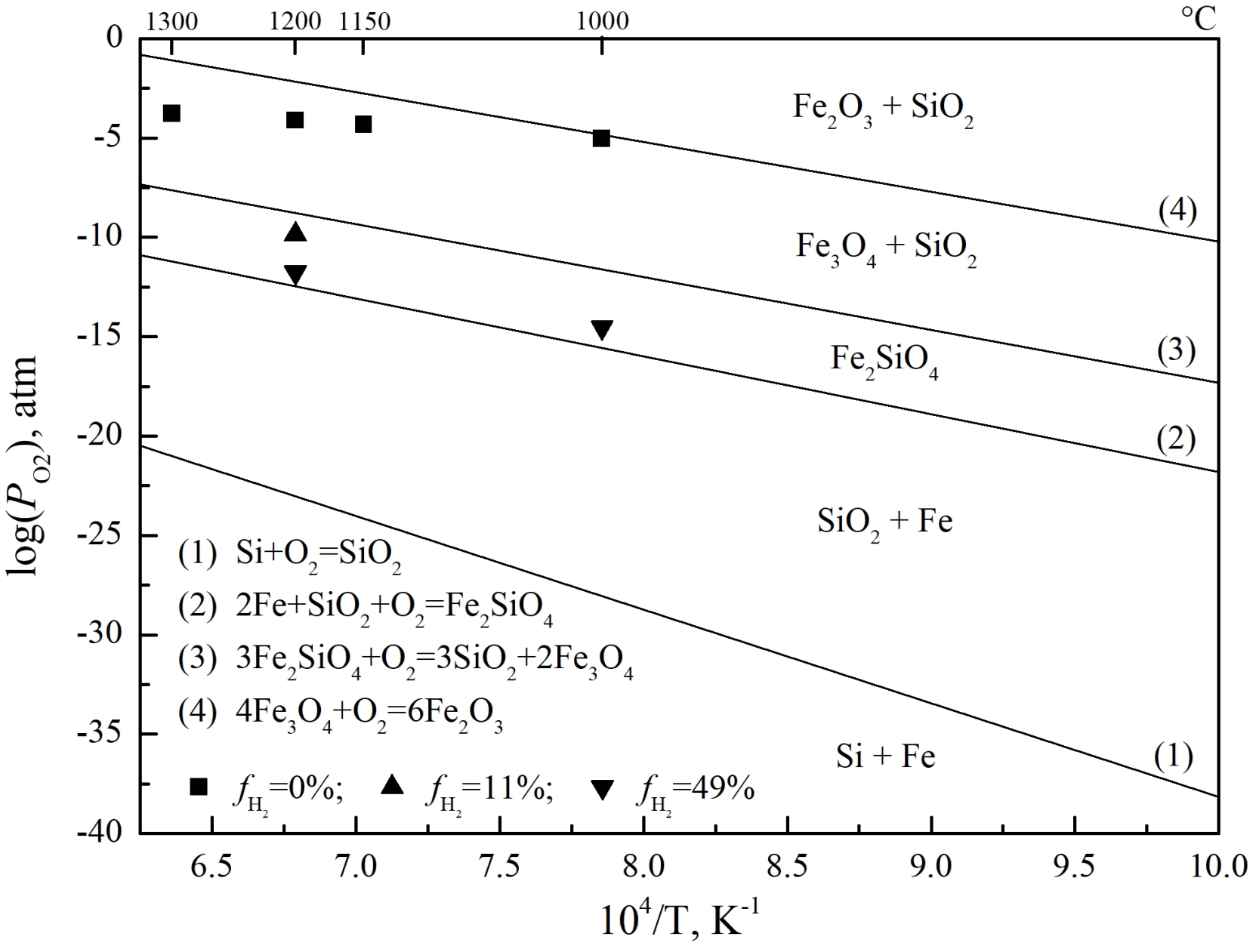
1300
1200
1150
1000
°C
0
-5
-10
-15
-20
-25
-30
-35
-40
log(P_{O2}), atm
$Fe_2O_3 + SiO_2$
$Fe_3O_4 + SiO_2$
Fe_2SiO_4
$SiO_2 + Fe$
Si + Fe
(4)
(3)
(2)
(1)
(1) $Si+O_2=SiO_2$
(2) $2Fe+SiO_2+O_2=Fe_2SiO_4$
(3) $3Fe_2SiO_4+O_2=3SiO_2+2Fe_3O_4$
(4) $4Fe_3O_4+O_2=6Fe_2O_3$
f_{H_2}=0%; f_{H_2}=11%; f_{H_2}=49%
6.5
7.0
7.5
8.0
8.5
9.0
9.5
10.0
10^4/T, K^{-1}

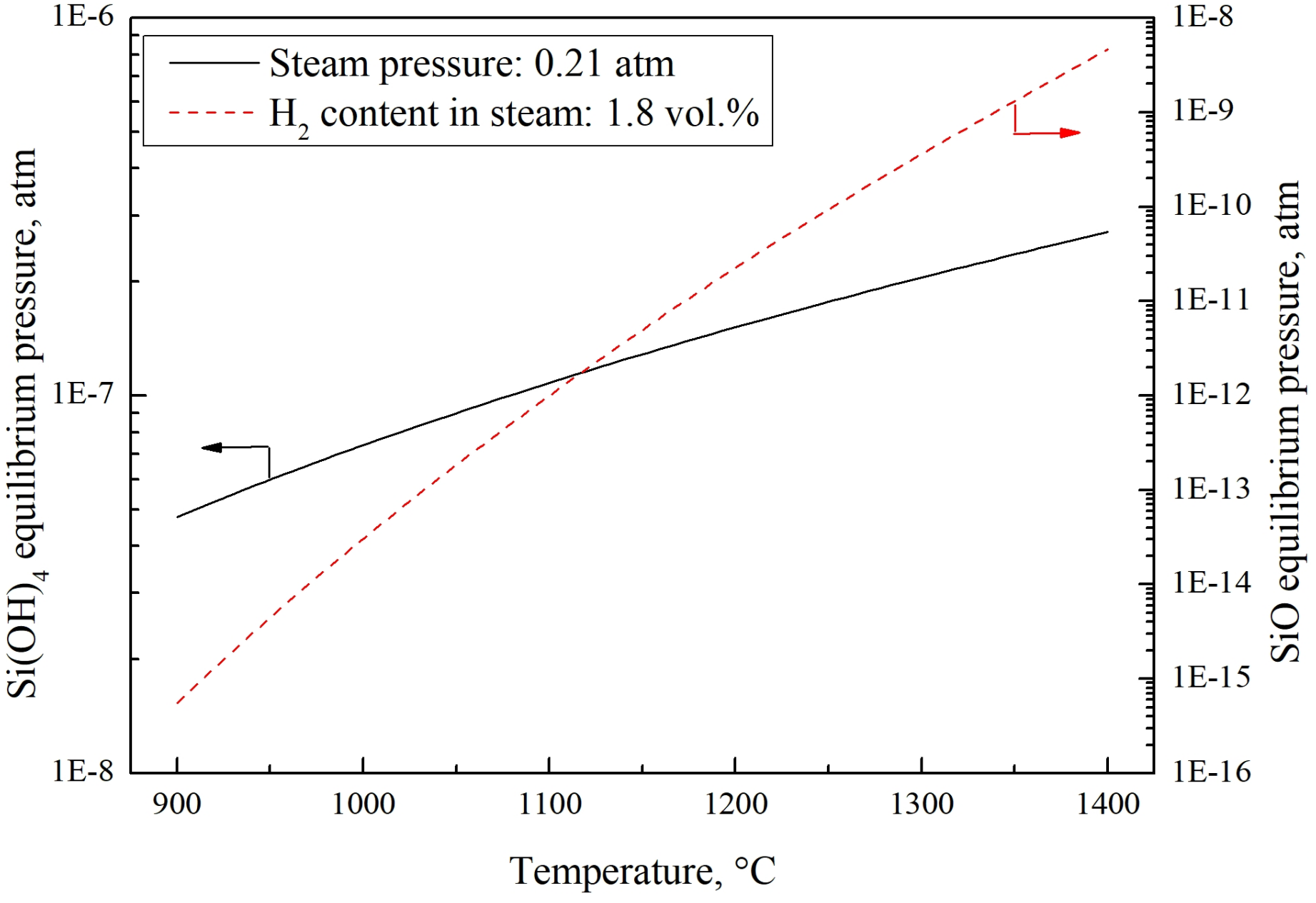
Steam pressure: 0.21 atm
H2 content in steam: 1.8 vol.%
Si(OH)4 equilibrium pressure, atm
SiO equilibrium pressure, atm
Temperature, °C
1E-6
1E-7
1E-8
1E-8
1E-9
1E-10
1E-11
1E-12
1E-13
1E-14
1E-15
1E-16
900
1000
1100
1200
1300
1400

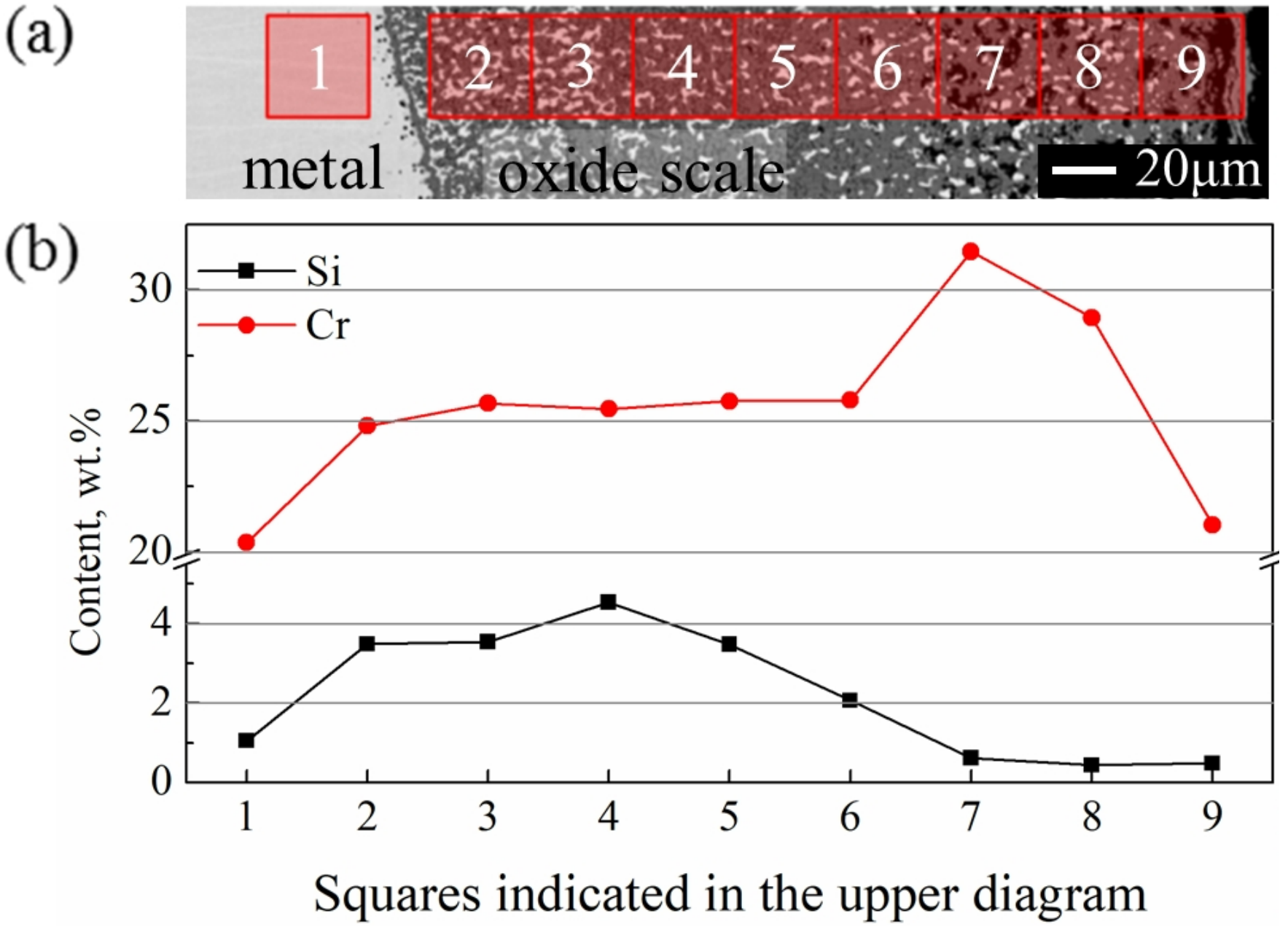
(a)
1
2
3
4
5
6
7
8
9
metal
oxide scale
20μm
(b)
Si
Cr
Content, wt.%
30
25
20
4
2
0
1
2
3
4
5
6
7
8
9
Squares indicated in the upper diagram

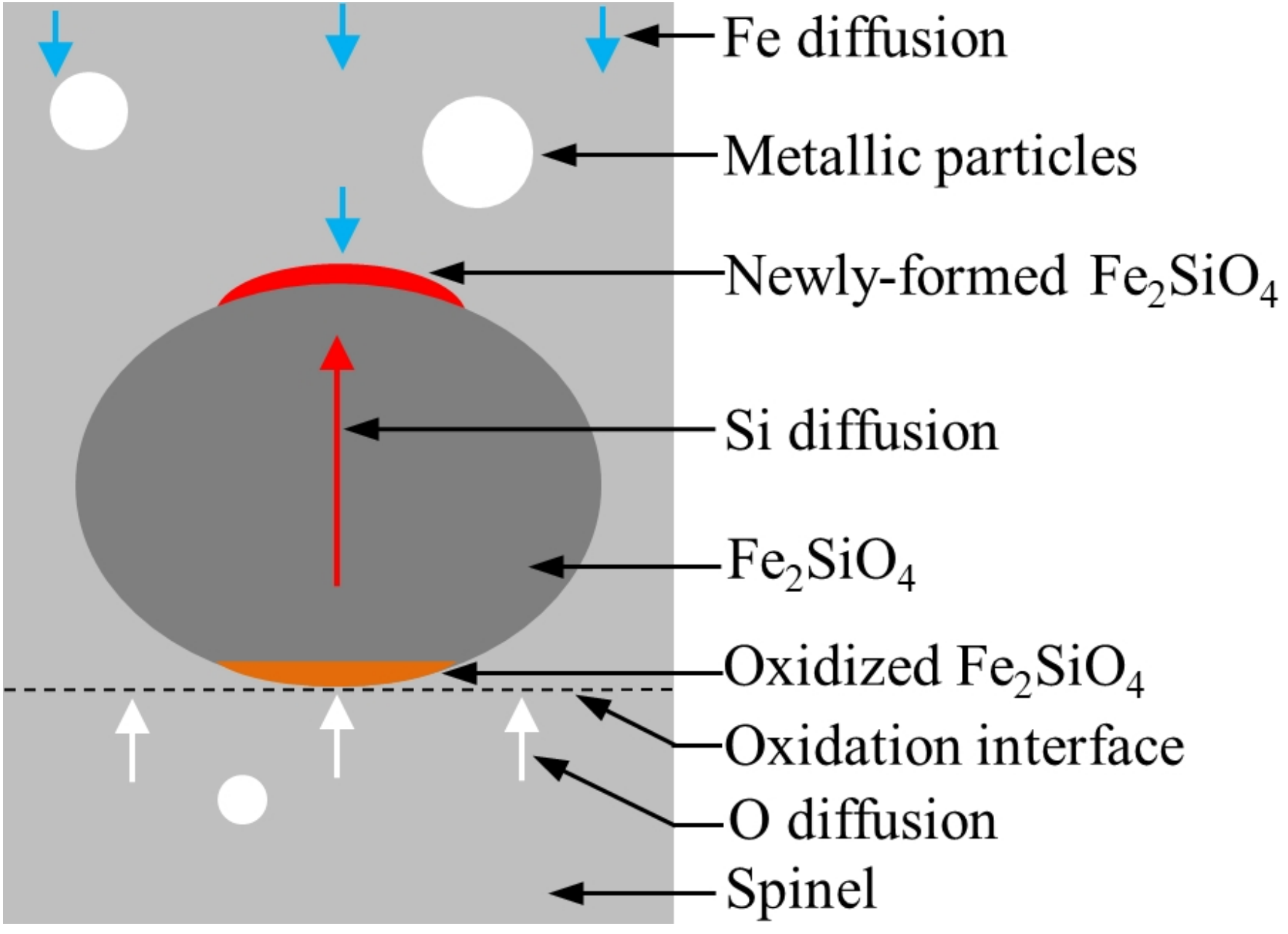
Fe diffusion
Metallic particles
Newly-formed Fe_2SiO_4
Si diffusion
Fe_2SiO_4
Oxidized Fe_2SiO_4
Oxidation interface
O diffusion
Spinel